

**UNCLASSIFIED**

**AD 410299**

**DEFENSE DOCUMENTATION CENTER**

**FOR**

**SCIENTIFIC AND TECHNICAL INFORMATION**

**CAMERON STATION, ALEXANDRIA, VIRGINIA**



**UNCLASSIFIED**

NOTICE: When government or other drawings, specifications or other data are used for any purpose other than in connection with a definitely related government procurement operation, the U. S. Government thereby incurs no responsibility, nor any obligation whatsoever; and the fact that the Government may have formulated, furnished, or in any way supplied the said drawings, specifications, or other data is not to be regarded by implication or otherwise as in any manner licensing the holder or any other person or corporation, or conveying any rights or permission to manufacture, use or sell any patented invention that may in any way be related thereto.

N-63-4-3

NAVWEPS REPORT 7941  
Part 1  
NOTS TP 2977  
COPY 60

## COMPARISON OF THEORY AND EXPERIMENT FOR VENTED HYDROFOILS

### Part 1. ANALYSIS

By

Andrew G. Fabula

Research Department

Released to ASTIA for further dissemination with  
out limitations beyond those imposed by security  
regulations.

**ABSTRACT.** The work of ~~three preceding reports~~ on the linearized theory of vented hydrofoils is completed by a detailed exposition of the procedure for calculating hydrodynamic coefficients. The basic assumption is steady, plane potential flow with two free streamlines; one detaching at an arbitrary chordwise position and the other detaching at the trailing edge. The single cavity terminates at an arbitrary distance downstream of the trailing edge. The calculation of the key smooth-entry, open-model parameters is illustrated by considering a symmetrical and a cambered profile, each vented at 30% chord. The theoretical  $C_D$  and  $C_L$  curves for two vented hydrofoils with exhaust at 30% chord are compared with water-tunnel test data. The agreement is not as good as in previous comparisons for leading-edge or trailing-edge free-streamline detachment. Real-fluid and tunnel blockage effects are believed to have produced the discrepancies. Because the calculations for arbitrary profile involve functions that are independent of profile form, the function tables that were generated during this work are given in Part 2 of this report, bound separately.



U. S. NAVAL ORDNANCE TEST STATION

China Lake, California

March 1963

AS AD No. 410299  
BY UDC

410299

# U. S. NAVAL ORDNANCE TEST STATION

AN ACTIVITY OF THE BUREAU OF NAVAL WEAPONS

C. BLENNMAN, JR., CAPT., USN  
Commander

WM. B. MCLEAN, PH.D.  
Technical Director

## CONTENTS

Foreword . . . . .	iii
Notation . . . . .	v
Introduction . . . . .	1
Infinite Cavity Length . . . . .	2
NACA 0010 Thickness Distribution . . . . .	5
Polynomial and Uniform-Load Camber Lines . . . . .	6
Hydrofoil B . . . . .	10
The Smooth-Entry, Open-Model Parameters . . . . .	10
NACA 0010 Thickness Distribution . . . . .	16
Uniform-Load Camber Line . . . . .	22
The Flat-Plate Parameters . . . . .	24
Open Model . . . . .	24
Closed Model . . . . .	26
Discussion . . . . .	27
Examples of Theoretical $C_L$ and $C_D$ Versus $K$ and Two Comparisons of Theory and Experiment . . . . .	30
Hydrofoil A . . . . .	30
Hydrofoil B . . . . .	35
Discussion . . . . .	35
Summary . . . . .	40
Appendixes:	
A. Corrigenda . . . . .	41
B. Vented Wedge . . . . .	42
C. Partly Closed Model Solutions for Vented Flat Plate . . . . .	48
References . . . . .	52

NOTS Technical Publication 2977

NA VWEPS Report 7941, Part 1

Published by . . . . . Research Department  
Manuscript . . . . . P5006/MS-7  
Collation . . . . . Cover, 30 leaves, abstract cards  
First printing . . . . . 255 numbered copies  
Security classification . . . . . UNCLASSIFIED

## FOREWORD

As one of a series on vented hydrofoils, this report, consisting of two parts, completes the application of linearized theory for steady, plane, unbounded flow. The general study is motivated by the possible use of gas exhaust for torpedo-control purposes and the use of base-vented hydrofoils as propeller blades.

The theoretical calculations are illustrated by treating two vented hydrofoils for which experimental results were given in Water-Tunnel Tests of Hydrofoils With Forced Ventilation, by T. G. Lang, D. A. Daybell, and K. E. Smith (NAVORD Report 7008, 10 November 1959).

The comparison of theory with experiment leads to new insight into the nature of the experimental flows.

Because the calculations for arbitrary profile involve functions that are independent of profile form, the function tables that were generated during this work are given in Part 2 of this report, bound separately. Thus other researchers may consider further hydrofoil profiles with minimal labor. However, since the tables are of restricted interest, Part 2 is being sent only to a small number of those receiving Part 1. Others who wish to receive Part 2 may write to Commander, U. S. Naval Ordnance Test Station, China Lake, Calif., Attn: Code 7506.

This work was done under Bureau of Naval Weapons Task Assignments RUAW-4E401/216 1/R009-01-003 and RUTO-3E-000/216 1/R009-01-003, problem assignment 401. The report was reviewed for technical adequacy by Dr. Blaine R. Parkin of the RAND Corp.

Released by  
T. E. PHIPPS, Head,  
Research Department  
20 March 1963

Under authority of  
Wm. B. McLEAN  
Technical Director

# NOTATION

$a$	$\frac{\sqrt{l-e} - \sqrt{(l-1)e}}{\sqrt{l-e} + \sqrt{(l-1)e}}$
$b$	$(1+a)\sqrt{l-1}$
$a_1 + ib_1, a_2 + \dots$	Coefficients in expansion of $w(z)$ for $z \rightarrow \infty$
$c + id$	$\zeta_\infty = Ae^{i\lambda}$
$c_n$	$c_n = \frac{2}{\pi} \int_0^\pi H(\theta) \cos n\theta \, d\theta, \quad n = 1, 2, \dots$
$C'$	Closure coefficient
$C_z$	z-plane closure singularity coefficient
$C_D, C_L, C_M$	Drag, lift, and moment coefficients for unit chord length and unit span (Fig. 1)
$C_Q$	Gas-supply coefficients, taken from Ref. 11
$d_n$	$c_n + 2(a - a_g) \cos n\theta'$
$e$	Exhaust location measured from leading edge for unit chord length
$F, G$	Functions of $c, d$ , and $\cos \theta$ (page 12)
$F_1, F_2, F_3, F_4$	Functions of $c, d$ , and $\cos \theta$ (page 12)
$h$	Hydrofoil contour height above x axis
$h', h''$	Parameters in polynomial approximation of uniform-load camber line
$H$	Contour slope, $dh \pm / dx$
$i$	$\sqrt{-1}$
$I_n$	$\int_0^{\theta'} \left( \frac{\cos \theta - \cos \theta'}{1 + \cos \theta'} \right)^n d\theta$

Im.	Imaginary part of
$J_n$	$\int_{\theta'}^{\pi} \left( \frac{\cos \theta - \cos \theta'}{1 + \cos \theta'} \right)^n d\theta$
K	Cavity number, $2(p_{\infty} - p_c)/\rho U_{\infty}^2$
$l$	Distance from leading edge to cavity-termination point, called cavity length
$M_n$	$I_n - J_n$
$Ne^{iv}$	$\zeta_{\infty} - (a + ib) = c - a + i(d - b)$
P	Vented flat-plate solution for unit angle of attack and open-cavity model
$P_n$	$I_n + J_n$
Q	Vented flat-plate solution for unit angle of attack and closed-cavity model
Re.	Real part of
$t_w$	Wake thickness for unit chord
T	$t_w/t_{w0}$
u, v	x and y components of velocity perturbation divided by $U_{\infty}$
w	Conjugate complex perturbation velocity, $u - iv$ , and analytic function of $z$ and $\zeta$
x, y	Cartesian coordinates in physical plane with free stream in positive x direction and (0, 0) at leading edge
z	$x - iy$
$\alpha$	Angle of attack
$\beta$	Flat-plate solution parameter
$\gamma_0, \gamma_1 \dots$	Parameters in polynomial approximation of uniform-load camber line
$\delta$	Vented wedge full apex angle

## **NAVWEPS REPORT 7941**

### **Part I**

$\delta_{-1/2}, \delta_0, \delta_1, \dots$	Parameters in expression for NACA 0010 profile slope distribution
$\zeta$	Circle-plane complex coordinate, $\zeta = \zeta_1 + i\zeta_2$
$\theta$	Circle-plane polar angle
$\theta'$	Value of $\theta$ at leading-edge point on unit circle
$\lambda, \Lambda$	$\zeta_\infty = Ae^{i\lambda}$
$\nu, N$	$\zeta_\infty - (a + ib) = Ne^{i\nu}$
$\rho$	Water density
$\tau$	Tunnel height divided by hydrofoil chord
$\psi (\psi')$	$\text{Arctan} [d + (-)\sqrt{1 - a^2}] / (c - a)$

### **Subscripts**

c	Cavity value
cl	Closed model
cw	Cavity-wall-speed linearization
fs	Free-stream-speed linearization
o	Open model
P	Open-model flat-plate solution for unit angle of attack
Q	Closed-model flat-plate solution for unit angle of attack
s	Smooth-entry condition for open model
$\pm$	Respectively upper and lower sides of singularity slit or hydrofoil
$\infty$	Condition or value at $z = \infty$

### **Superscripts**

+	Cusp closure
0	Zero angle of attack
-	Thickness profile and its parameters after removal of leading-edge singularity
~	Open-model point-drag profile and its parameters



## INTRODUCTION

Theoretical analyses of vented hydrofoils using the linearized "thin-airfoil" theory of steady, plane, ideal flow are presented in Ref. 1 and 2. This third report presents sample theoretical results, comparison with experiment, and function tables with which hydrodynamic coefficients can be calculated according to the formulas developed in Ref. 1 and 2.

The assumed flow configuration is shown in Fig. 1, where the unit-chord profile has a full cavity (i. e.,  $l > 1$ ) and the more forward free-streamline detachment point, without loss of generality, is assumed to be on the upper side. Thus positive lift is directed away from the foil on the vented side, and positive moment tends to rotate the foil so as to shield the vented side from the free stream.

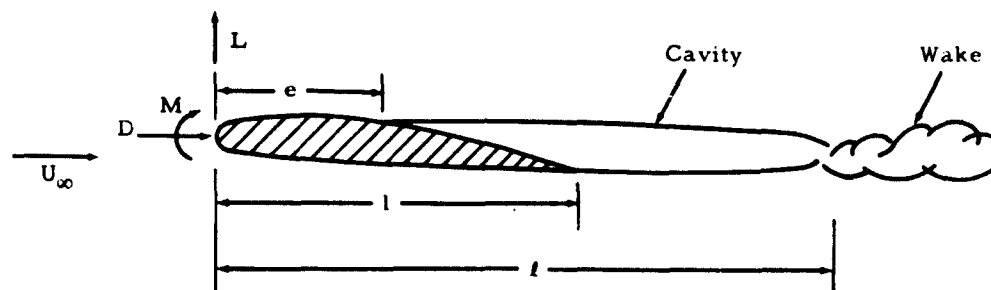


FIG. 1. Typical Vented Hydrofoil Flow Configuration for a Full Cavity.

The tables in Part 2 of this report are in four groups. Tables 1 through 4 give functions convenient for treating  $C_D$ ,  $C_L$ , and  $C_M$  for a broad class of profiles for  $l = \infty$ . Tables 5 through 8 give the functions  $F_1$ ,  $F_2$ ,  $F_3$ , and  $F_4$  that are multiplied by a profile's wetted contour slope distribution and then integrated to obtain the profile's key parameters (neglecting moment) of  $\alpha_s$ ,  $u_{cs}$ ,  $t_{ws}$ , and  $C_{Ls}$ . These integrations are for nine values of  $l$  from  $\infty$  to 1.1. Table 9 gives  $x(\theta)$  which is used to transfer the profile slope to the unit circle for the integrations. Auxiliary tables useful in the calculations and in possible future work are Tables 10 through 14. Tables 15 through 20 allow calculation of  $C_D$ ,  $C_L$ , and  $K$  versus  $l$  for the arbitrary profile at arbitrary attack angle.

In this work, the exhaust point location,  $e$ , is in effect assumed to be in the range  $0 \leq e < 1$ , since for trailing-edge venting,  $e = 1$ , the work in Ref. 3 is complete in itself. However, for various reasons, particularly the arrangement of tables, the case of  $e = 1$  is also included here at several points.

### INFINITE CAVITY LENGTH

In Ref. 2 the relations for hydrodynamic coefficients for  $l = \infty$  are applied mainly to profiles of simple form. The function tables given here allow ready treatment of a fairly broad class of profiles.

The relations for  $l = \infty$  are

$$(1) \quad \begin{aligned} C_D &= \frac{\pi}{2} \left( \frac{1 + \sqrt{e}}{2} \right)^2 d_1^2, & C_L &= \pi \left( \frac{1 + \sqrt{e}}{2} \right)^2 (2d_1 \cos \theta' - d_2) \\ C_M &= \frac{\pi}{4} \left( \frac{1 + \sqrt{e}}{2} \right)^4 \left[ d_4 - 6 \cos \theta' d_3 + 2(1 + 6 \cos^2 \theta') d_2 \right. \\ &\quad \left. - 2 \cos \theta' (3 + 4 \cos^2 \theta') d_1 \right]^* \end{aligned}$$

The  $d_n$  coefficients are determined by the contour slope and the angle of attack  $\alpha$ , with

$$(2) \quad \begin{aligned} d_n &= c_n + 2(\alpha - \alpha_s) \cos n\theta', & c_n &= \frac{2}{\pi} \int_0^\pi \cos n\theta H d\theta \quad (n = 1, 2, \dots) \\ \alpha_s &= \frac{1}{\pi} \int_0^\pi H d\theta, & \cos \theta' &= \frac{1 - \sqrt{e}}{1 + \sqrt{e}} = a \end{aligned}$$

It is to be noted that  $\alpha_s$ , the smooth-entry attack angle, is denoted by  $\alpha_0$  in Ref. 2, but in this report the subscript  $o$  is reserved for the open-model condition.  $H(\theta)$  is the wetted-surface contour slope distribution,  $dh_\pm/dx$ , specified over the upper half of the  $\zeta$ -plane unit circle. The upper surface (+) corresponds to  $0 \leq \theta < \theta'$ , and the lower surface (-) corresponds to  $\theta' < \theta \leq \pi$ , according to the wetted-surface mapping for  $l = \infty$ ,

$$(3) \quad \sqrt{x} = \pm \left( \frac{1 + \sqrt{e}}{2} \right) (\cos \theta - \cos \theta') = \pm \left( \frac{\cos \theta - \cos \theta'}{1 + \cos \theta'} \right) = \pm \left( \frac{\cos \theta - a}{1 + a} \right)$$

\* See Item 1, Appendix A.

It will be seen later that these uses of  $a_s$  and  $a$  for  $l = \infty$  are consistent with the definitions of the same symbols for finite  $l$ . For each profile and  $l$ ,  $a - a_s$  is important to the character of the pressure distribution near the leading edge, and thus  $a_s$  is a useful parameter. Therefore, for continuity between the results for infinite and finite  $l$ , the formulas of Eq. 1 are put in the form

$$C_D = \left[ \sqrt{C_{D_s}} + (a - a_s) \sqrt{2\pi} \left( \frac{1 - \sqrt{e}}{2} \right) \right]^2, \quad C_L = C_{L_s} + 2\pi(a - a_s) \left( \frac{1 + \sqrt{e}}{2} \right)^2$$

$$(4) \quad C_M = C_{M_s} - \frac{\pi}{2} (a - a_s) \left( \frac{1 + \sqrt{e}}{2} \right)^4 \left[ 1 + 4 \left( \frac{1 - \sqrt{e}}{1 + \sqrt{e}} \right)^2 \right]^*$$

The smooth-entry-angle parameters are seen to be

$$(5) \quad \sqrt{C_{D_s}} = \sqrt{\frac{2}{\pi}} \left( \frac{1 + \sqrt{e}}{2} \right) \int_0^\pi \cos \theta H d\theta$$

$$(6) \quad C_{L_s} = 2 \left( \frac{1 + \sqrt{e}}{2} \right)^2 \int_0^\pi (2 \cos \theta' \cos \theta - \cos 2\theta) H d\theta$$

$$(7) \quad C_{M_s} = \frac{1}{2} \left( \frac{1 + \sqrt{e}}{2} \right)^4 \int_0^\pi [\cos 4\theta - 6 \cos \theta' \cos 3\theta + 2(1 + 6 \cos^2 \theta') \cos 2\theta - 2 \cos \theta' (3 + 4 \cos^4 \theta') \cos \theta] H d\theta$$

When only the results for  $l = \infty$  are of interest, the natural formulation in terms of zero angle of attack is

$$(8) \quad C_D = \left[ \sqrt{C_D^0} + a \sqrt{2\pi} \left( \frac{1 - \sqrt{e}}{2} \right) \right]^2, \quad C_L = C_L^0 + 2\pi a \left( \frac{1 + \sqrt{e}}{2} \right)^2$$

$$C_M = C_M^0 - \frac{\pi}{2} a \left( \frac{1 + \sqrt{e}}{2} \right)^4 \left[ 1 + 4 \left( \frac{1 - \sqrt{e}}{1 + \sqrt{e}} \right)^2 \right]$$

Noting that  $d_n = c_n$  for  $a = a_s$ , and using the relations

\* See Item 3, Appendix A.

$$\cos 2\theta - \cos 2\theta' = 4a (\cos \theta - a) + 2 (\cos \theta - a)^2$$

$$\cos 3\theta - \cos 3\theta' = (12a^2 - 3)(\cos \theta - a) + 12a (\cos \theta - a)^2 + 4(\cos \theta - a)^3$$

$$\begin{aligned} \cos 4\theta - \cos 4\theta' &= (32a^3 - 16a)(\cos \theta - a) + (48a^2 - 8)(\cos \theta - a)^2 \\ &\quad + 32a (\cos \theta - a)^3 + 8 (\cos \theta - a)^4 \end{aligned}$$

obtain

$$(9) \quad \sqrt{C_D^0} = \sqrt{\frac{2}{\pi}} \int_0^\pi \left( \frac{\cos \theta - a}{1 + a} \right) H d\theta$$

$$(10) \quad C_L^0 = -4 \left[ \left( \frac{a}{1 + a} \right) \int_0^\pi \left( \frac{\cos \theta - a}{1 + a} \right) H d\theta + \int_0^\pi \left( \frac{\cos \theta - a}{1 + a} \right)^2 H d\theta \right]$$

$$\begin{aligned} C_M^0 &= 2 \left[ \frac{a}{(1 + a)^3} \int_0^\pi \left( \frac{\cos \theta - a}{1 + a} \right) H d\theta - \frac{1}{(1 + a)^2} \int_0^\pi \left( \frac{\cos \theta - a}{1 + a} \right)^2 H d\theta \right. \\ &\quad \left. + \left( \frac{2a}{1 + a} \right) \int_0^\pi \left( \frac{\cos \theta - a}{1 + a} \right)^3 H d\theta + 2 \int_0^\pi \left( \frac{\cos \theta - a}{1 + a} \right)^4 H d\theta \right]^* \end{aligned}$$

Because of the form of  $x(\theta)$  in Eq. 3, any term in  $H(\theta)$  proportional to  $(\sqrt{x})^m$ , where  $m$  is an integer, leads to integrals of the form

$$\text{Upper side: } I_n = \int_0^{\theta'} \left( \frac{\cos \theta - a}{1 + a} \right)^n d\theta$$

$$\text{Lower side: } J_n = \int_{\theta'}^\pi \left( \frac{\cos \theta - a}{1 + a} \right)^n d\theta$$

The integer exponent  $n$  equals  $m + 1$  in  $\sqrt{C_D^0}$ ,  $m + 1$  or  $m + 2$  in  $C_L^0$ , and  $m + 1$  through  $m + 4$  in  $C_M^0$ . Tables 1 through 4 in Part 2 give  $I_n$ ,  $J_n$ ,  $P_n = I_n + J_n$ , and  $M_n = I_n - J_n$  for  $m = 1$  through 10 and for  $\theta'$  values corresponding to  $e = 0, 0.025, 0.05, 0.1, 0.2, \dots, 1.0$  plus two additional values of  $e = 0.00516$  and  $0.01754$  corresponding to  $\theta' = 30^\circ$  and  $40^\circ$ . The evenly spaced values are the same as those used in the later tables for finite  $l$ . The two extra  $e$  values help define the behavior for  $e \rightarrow 0$ , which can be very nonlinear, as discussed in Ref. 2.

\* See Item 4, Appendix A

The use of these tables will be illustrated by treating typical thickness and camber distributions.

### NACA 0010 THICKNESS DISTRIBUTION

The first example is the NACA four-digit series basic thickness which has the form (Ref. 4)

$$h_{\pm} = \pm 5t(0.2969 x^{\frac{1}{2}} - 0.1260x - 0.3516x^2 + 0.2843x^2 - 0.1015x^4)$$

where  $t$  is the maximum thickness-to-chord ratio. Thus for the NACA 0010 profile,

$$(12) \quad \frac{dh_{\pm}}{dx} = \pm \left( \delta_{-\frac{1}{2}} x^{-\frac{1}{2}} + \delta_0 + \delta_1 x + \delta_2 x^2 + \delta_3 x^3 \right)$$

where

$$\delta_{-\frac{1}{2}} = 0.074225, \quad \delta_0 = -0.06300, \quad \delta_1 = -0.35160$$

$$\delta_2 = 0.42645, \quad \delta_3 = 0.20300$$

The resultant expressions for  $\sqrt{C_D^0}$ ,  $C_L^0$ , and  $C_M^0$  are

$$(13) \quad C_D^0 = \sqrt{\frac{2}{\pi}} \left( \delta_{-\frac{1}{2}} P_0 + \delta_0 M_1 + \delta_1 M_3 + \delta_2 M_5 + \delta_3 M_7 \right)$$

$$(14) \quad C_L^0 = -4 \left( \frac{a}{1+a} \sqrt{\frac{\pi}{2}} \sqrt{C_D^0} + \delta_{-\frac{1}{2}} P_1 + \delta_0 M_2 + \delta_1 M_4 + \delta_2 M_6 + \delta_3 M_8 \right)$$

$$(15) \quad C_M^0 = 4 \left[ \frac{a}{(1+a)^3} \sqrt{\frac{\pi}{2}} \sqrt{C_D^0} + \frac{1}{8(1+a)^2} C_L^0 \right. \\ \left. + \frac{a}{1+a} \left( \delta_{-\frac{1}{2}} P_2 + \delta_0 M_3 + \delta_1 M_5 + \delta_2 M_7 + \delta_3 M_9 \right) \right. \\ \left. + \delta_{-\frac{1}{2}} P_3 + \delta_0 M_4 + \delta_1 M_6 + \delta_2 M_8 + \delta_3 M_{10} \right]$$

Since the  $\pm \delta_{-\frac{1}{2}} x^{-\frac{1}{2}}$  component in  $H$  corresponds to the point-drag profile slope for  $l = \infty$ , there should be no contribution from this term to  $C_L^0$  and  $C_M^0$ . This is seen to be true using, in Eq. 14,

$$P_1 + \frac{a}{1+a} P_0 = -\frac{a\pi}{1+a} + \frac{a}{1+a} (\pi) = 0$$

and in Eq. 15,

$$\frac{a}{(1+a)^3} P_0 + \frac{a}{1+a} P_2 + P_3 = \frac{a}{(1+a)^3} \pi + \frac{a}{1+a} \left[ \frac{\pi(1/2 - a^2)}{(1+a)^2} \right] - \frac{a\pi(3/2 + a^2)}{(1+a)^3} = 0$$

Thus, simplified forms for the 0010 profile are

$$(13') \quad \sqrt{C_D^0} = \sqrt{\frac{2}{\pi}} \left( \pi \delta_{-\frac{1}{2}} + \delta_0 M_1 + \delta_1 M_3 + \delta_2 M_5 + \delta_3 M_7 \right)$$

$$(14') \quad C_L^0 = -4 \left[ \frac{a}{1+a} \left( \sqrt{\frac{\pi}{2}} \sqrt{C_D^0} - \pi \delta_{-\frac{1}{2}} \right) + \delta_0 M_2 + \delta_1 M_4 + \delta_2 M_6 + \delta_3 M_8 \right]$$

$$(15') \quad C_M^0 = 4 \left[ \frac{a}{(1+a)^3} \left( \sqrt{\frac{\pi}{2}} \sqrt{C_D^0} - \pi \delta_{-\frac{1}{2}} \right) + \frac{1}{8(1+a)^2} C_L^0 \right. \\ \left. + \frac{a}{1+a} \left( \delta_0 M_3 + \delta_1 M_5 + \delta_2 M_7 + \delta_3 M_9 \right) \right. \\ \left. + \delta_0 M_4 + \delta_1 M_6 + \delta_2 M_8 + \delta_3 M_{10} \right]$$

Figure 2 gives the resultant curves of  $\sqrt{C_D^0}$ ,  $C_L^0$ , and  $C_M^0$  versus  $e$ , obtained via Tables 3 and 4. For another thickness ratio,  $t'$ ,

$$(16) \quad \left( \sqrt{C_D^0} \right)_{t'} = 10 t' \left( \sqrt{C_D^0} \right)_{0010}$$

and the analogous forms for  $C_L^0$  and  $C_M^0$ .

#### POLYNOMIAL AND UNIFORM-LOAD CAMBER LINES

The second example is the fourth-order polynomial camber line, with

$$h_{\pm} = \gamma_0 x + \frac{\gamma_1}{2} x^2 + \frac{\gamma_2}{3} x^3 + \frac{\gamma_3}{4} x^4, \quad \frac{dh_{\pm}}{dx} = \gamma_0 + \gamma_1 x + \gamma_2 x^2 + \gamma_3 x^3$$

and thus (not considering moment),

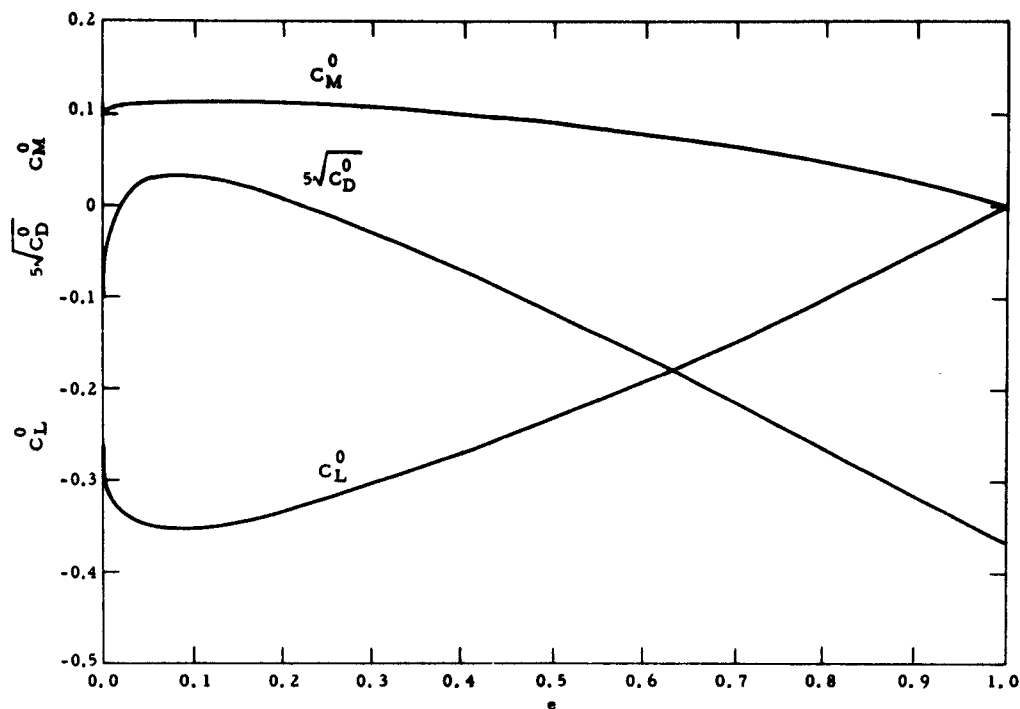


FIG. 2. Infinite-Cavity Drag, Lift, and Moment Functions for NACA 0010 Profile.

$$(17) \quad \sqrt{C_D^0} = \sqrt{\frac{2}{\pi}} (\gamma_0 P_1 + \gamma_1 P_3 + \gamma_2 P_5 + \gamma_3 P_7)$$

$$C_L^0 = -4 \left( \frac{a}{1+a} \sqrt{\frac{\pi}{2}} \sqrt{C_D^0} + \gamma_0 P_2 + \gamma_1 P_4 + \gamma_2 P_6 + \gamma_3 P_8 \right)$$

In Ref. 2, this type of camber line was used to approximate the uniform-load or NACA "a = 1.0" mean line (Ref. 4) by fitting the polynomial to the mean line for design  $C_L$  of 1.0 to give

$x = 0,$	$h_{\pm} = 0$
$= 0.25,$	$= 0.04475 = h'$
$= 0.50,$	$= 0.05515 = h''$
$= 0.75,$	$= 0.04475 = h'$
$= 1.00,$	$= 0$

The five-point fitting produces

$$\gamma_0 = -12 h' + \frac{64}{3} h'', \quad \gamma_1 = 152 h' - \frac{640}{3} h''$$

$$\gamma_2 = -384 h' + 512 h'', \quad \gamma_3 = -\frac{2}{3} \gamma_2$$

Figures 3 and 4 give  $\sqrt{C_D^0}$  and  $C_L^0$  versus  $e$  for the fourth-order polynomial approximation to the uniform-load camber line. Also shown are more accurate computer solutions for the precise uniform-load camber line, again for design  $C_L$  of 1.0. These were obtained by machine calculation, using the  $\sqrt{C_D^0}$  and  $C_L^0$  formulas expressed in terms of  $x$  instead of  $\theta$ :

$$\sqrt{C_D^0} = \frac{1}{\sqrt{2\pi}} \left\{ \int_0^e \left[ \sqrt{e} - (1 - \sqrt{e}) \sqrt{x} - x \right]^{-\frac{1}{2}} \frac{dh_+}{dx} dx \right. \\ \left. - \int_0^1 \left[ \sqrt{e} + (1 - \sqrt{e}) \sqrt{x} - x \right]^{-\frac{1}{2}} \frac{dh_-}{dx} dx \right\} \quad (18)$$

$$C_L^0 = -2 \left\{ \left( \frac{1 - \sqrt{e}}{2} \right) \sqrt{2\pi} \sqrt{C_D^0} + \int_0^e \sqrt{x} \left[ \sqrt{e} - (1 - \sqrt{e}) \sqrt{x} - x \right]^{-\frac{1}{2}} \frac{dh_+}{dx} dx \right. \\ \left. + \int_0^1 \sqrt{x} \left[ \sqrt{e} + (1 - \sqrt{e}) \sqrt{x} - x \right]^{-\frac{1}{2}} \frac{dh_-}{dx} dx \right\} \quad (19)$$

The machine calculations were made<sup>1</sup> on a Royal McBee LGP-30 digital computer by using uniform  $x$  increments of 0.005 and taking the integrand's value at the midpoint of each increment as its average. An important increase in accuracy was obtained by analytically correcting the increments adjoining the four singular points at  $x = 0$  and  $e$  in the upper-surface integrals and at  $x = 0$  and  $1$  in the lower-surface integrals. To calculate  $C_M^0$  in the same way,

<sup>1</sup> By J. A. Poore of this Station.



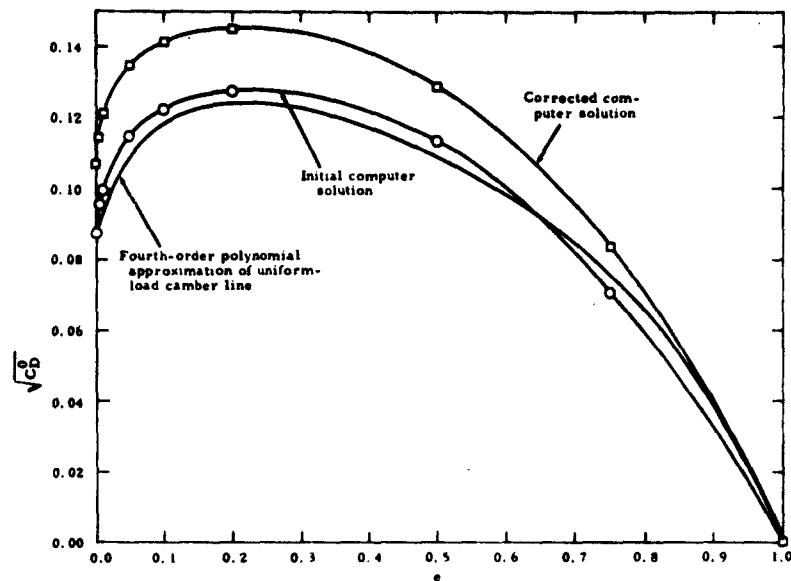


FIG. 3. Infinite-Cavity Drag Functions for Uniform-Load Camber Line and for Approximating Fourth-Order Polynomial Camber Line.

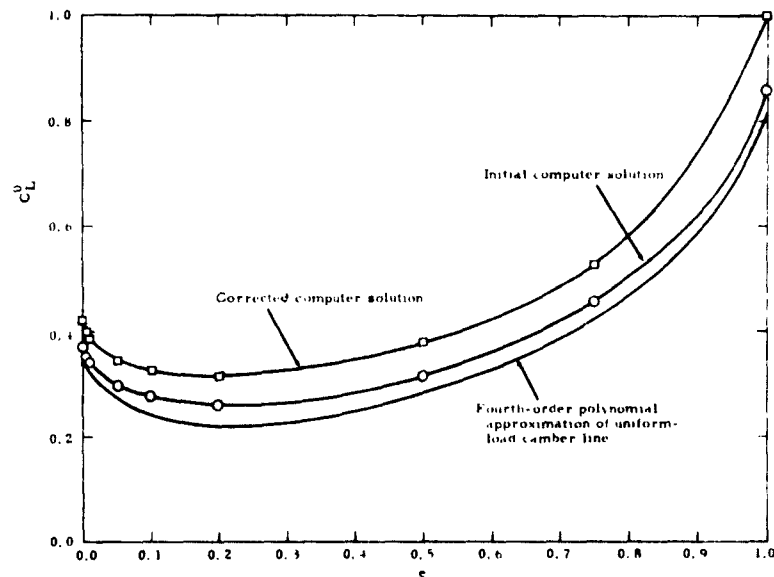


FIG. 4. Infinite-Cavity Lift Functions for Uniform-Load Camber Line and for Approximating Fourth-Order Polynomial Camber Line.

$$C_M^0 = \left( \frac{1 + \sqrt{e}}{2} \right)^2 \left[ (1 - \sqrt{e}) \sqrt{2\pi} \sqrt{C_D^0} + \frac{1}{2} C_L^0 \right] \\ + \int_0^e x(1 - \sqrt{e} + 2\sqrt{x}) \left[ \sqrt{e} - (1 - \sqrt{e})\sqrt{x} - x \right]^{-\frac{1}{2}} \frac{dh_+}{dx} dx \\ - \int_0^1 x(1 - \sqrt{e} - 2\sqrt{x}) \left[ \sqrt{e} + (1 - \sqrt{e})\sqrt{x} - x \right]^{-\frac{1}{2}} \frac{dh_-}{dx} dx$$

### HYDROFOIL B

The computer calculation was also used<sup>2</sup> to consider the NACA 652-015 profile, with modified trailing edge, called Hydrofoil B in Ref. 5. Figures 5 and 6 show the resultant  $\sqrt{C_D^0}$  and  $C_L^0$  for Hydrofoil B and for the approximation made to it in Ref. 2 by means of a roughly similar profile with a very simple contour expression.

### THE SMOOTH-ENTRY, OPEN-MODEL PARAMETERS

As derived and illustrated in Ref. 1, the treatment of an arbitrary profile for  $1 < l < \infty$  reduces in the main to calculating, for a spread of  $l$  values, the several parameters of the smooth-entry, open-model solution. When moment coefficient is not considered, four parameters are involved, whose formulas are

$$(20) \quad u_{cs} + ia_s = \frac{1}{\pi} \int_0^\pi \left[ \Lambda G + i \left( \frac{\Lambda^2 - 1}{2} \right) F \right] H d\theta$$

$$(21) \quad \frac{t_{ws}}{2\pi} + i \frac{C_{Ls}}{4\pi} = \frac{b l e^{-i\nu}}{N} \left\{ \frac{1}{\pi} \int_0^\pi \left[ \Lambda G + i \left( \frac{\Lambda^2 - 1}{2} \right) F \right]^2 H d\theta \right. \\ \left. - \frac{[2\Lambda^2 \sin 2\lambda + i(\Lambda^4 - 1)]}{(\Lambda^4 + 1 - 2\Lambda^2 \cos 2\lambda)} (u_{cs} + ia_s) \right\}$$

where

<sup>2</sup> By D. A. Daybell of this Station.

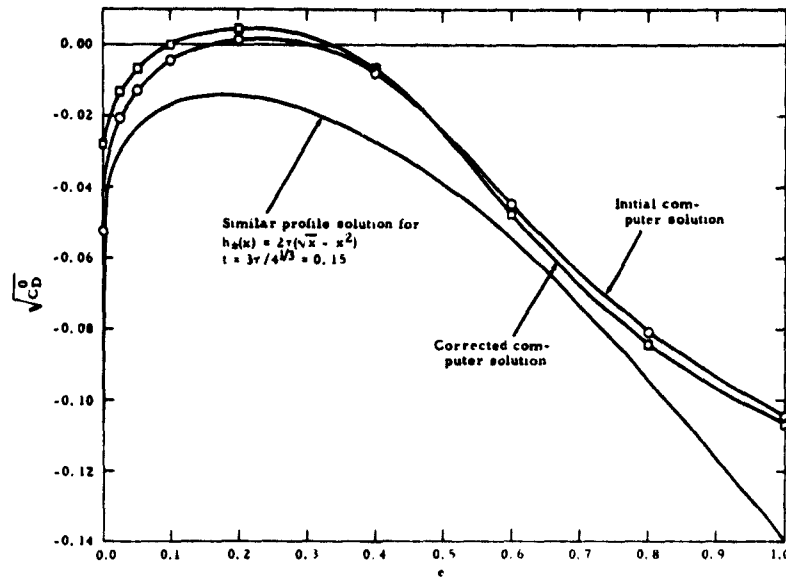


FIG. 5. Infinite-Cavity Drag Functions for Hydrofoil B and for Similar Profile of Simple Contour Expression.

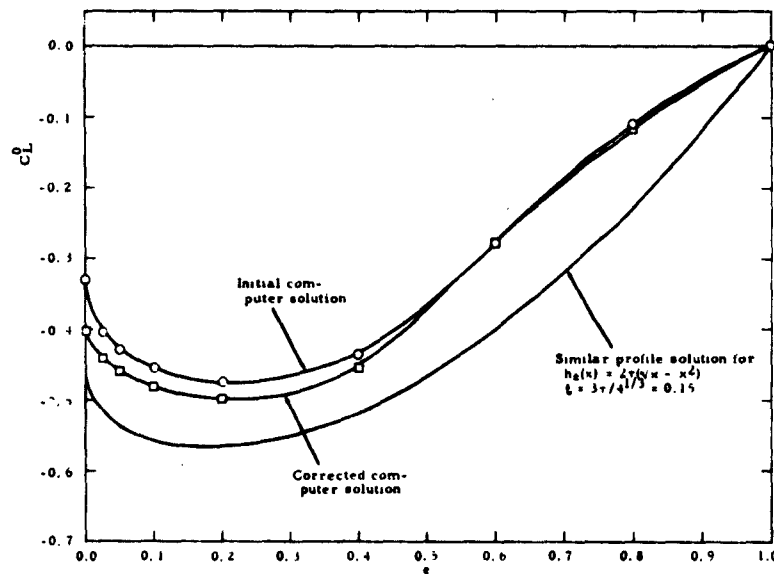


FIG. 6. Infinite-Cavity Lift Functions for Hydrofoil B and for Similar Profile of Simple Contour Expression.

$$F = \frac{1}{\Lambda^2 + 1 - 2\Lambda \cos(\lambda + \theta)} + \frac{1}{\Lambda^2 + 1 - 2\Lambda \cos(\lambda - \theta)}$$

$$= \frac{2(\Lambda^2 + 1) - 4\Lambda \cos \lambda \cos \theta}{(\Lambda^2 - 1)^2 - 4(\Lambda^2 + 1)\Lambda \cos \lambda \cos \theta + 4\Lambda^2(\cos^2 \lambda + \cos^2 \theta)}$$

and

$$G = \frac{\sin(\lambda + \theta)}{\Lambda^2 + 1 - 2\Lambda \cos(\lambda + \theta)} + \frac{\sin(\lambda - \theta)}{\Lambda^2 + 1 - 2\Lambda \cos(\lambda - \theta)}$$

$$= \frac{\sin \lambda [2(\Lambda^2 + 1) \cos \theta - 4\Lambda \cos \lambda]}{(\Lambda^2 - 1)^2 - 4(\Lambda^2 + 1)\Lambda \cos \lambda \cos \theta + 4\Lambda^2(\cos^2 \lambda + \cos^2 \theta)}$$

A desirable feature of these integrals is that there are no singularities in the integrand factors of H as long as  $1 < l \leq \infty$ . Thus if there are no singularities in H, or if they are removed as described in Ref. 1, the integrals can be evaluated by simple methods. The computations for this report were performed\* with an Ott rolling-disk planimeter. For more extensive studies, the calculation procedure given here could easily be adapted to machine computations.

During the course of the planimeter work, it was found worth while to shift to the following format:

$$(22) \quad \pi u_{cs} + i\pi a_s = \int_0^\pi (F_1 + iF_2) H d\theta$$

$$(23) \quad t_{ws} + \frac{iC_{Ls}}{2} = \frac{b\ell}{N} e^{-i\nu} \int_0^\pi (F_3 + iF_4) H d\theta$$

with

$$F_1 + iF_2 = \Lambda G + i \left( \frac{\Lambda^2 - 1}{2} \right) F$$

$$F_3 + iF_4 = (F_1 + iF_2) \left[ F_1 + iF_2 - \frac{2\Lambda^2 \sin 2\lambda + i(\Lambda^4 - 1)}{\Lambda^4 + 1 - 2\Lambda^2 \cos 2\lambda} \right]$$

---

\* By J. M. Hamilton of this Station.

$$= F_1^2 - F_2^2 + \frac{(\Lambda^4 - 1)F_2 - 2\Lambda^2 \sin 2\lambda F_1}{\Lambda^4 + 1 - 2\Lambda^2 \cos 2\lambda} + i \left[ 2F_1 F_2 + \frac{2\Lambda^2 \sin 2\lambda F_2 - (\Lambda^4 - 1)F_1}{\Lambda^4 + 1 - 2\Lambda^2 \cos 2\lambda} \right]$$

The use of  $F_3 + iF_4$  avoids some unnecessary compounding of errors, caused by subtracting nearly equal, relatively large terms, particularly for large  $l$ .

The planimeter work has considered the following spread of  $l$  values:

$$\infty, 8, 4, 2.5, 2, 1.5, 1.25, 1.125, \text{ and } 1.1$$

It will be seen that the absence of 1.0 from this list is regrettable, since the  $s$ -parameter curves, when plotted versus reciprocal cavity length, often show increasing curvature for  $l \rightarrow 1$ . The mapping used caused the forms of the  $s$ -parameter integrals to be indeterminate at  $l = 1$ , but it can be seen that the  $s$ -parameters are finite there unless the profile has a trailing-edge singularity. A case in which the solution for  $l = 1$  has been obtained is the vented wedge discussed in Appendix B. For more extensive work, it would be useful to specifically treat  $l = 1$  and to routinely obtain the smooth-entry, open-model relations for that limit. The  $l$  value of 1.125 could be dropped, keeping the number of cases to nine.

At the other limit,  $l = \infty$ , simplified relations are already available from the previous work. However, it is necessary to confirm that those previous results are recovered with the more general forms. Using the notation

$$\Lambda e^{i\lambda} = c + id = (a + N \cos \nu) + i(b + N \sin \nu)$$

and the definitions

$$a = \frac{\sqrt{l-e} - \sqrt{(l-1)e}}{\sqrt{l-e} + \sqrt{(l-1)e}}, \quad b = (1+a)\sqrt{l-1}$$

which lead to

$$N = (1+a) \sqrt{l} \left( \frac{l-1}{l-e} \right)^{\frac{1}{4}}, \quad \begin{pmatrix} \cos \\ \sin \end{pmatrix} \nu = \frac{1}{\sqrt{2}} \left[ 1 \mp \frac{\sqrt{l-1} \sqrt{l-e} + \sqrt{e}}{l} \right]^{\frac{1}{2}}$$

it can be seen that, for  $l \rightarrow \infty$ ,

$$(24) \quad c = 2 \left( \frac{1 - \sqrt{e}}{1 + \sqrt{e}} \right) + O(l^{-1}), \quad d = \left( \frac{4}{1 + \sqrt{e}} \right) \sqrt{l} [1 + O(l^{-1})]$$

The expressions for  $F_1, \dots, F_4$  in terms of  $c, d$ , and  $\cos \theta$  become

$$F_1 = \frac{d [2(c^2 + d^2 + 1) \cos \theta - 4c]}{(c^2 + d^2 - 1)^2 - 4(c^2 + d^2 + 1)c \cos \theta + 4c^2 + 4(c^2 + d^2) \cos^2 \theta}$$

$$F_2 = \frac{(c^2 + d^2 - 1)(c^2 + d^2 + 1 - 2c \cos \theta)}{(c^2 + d^2 - 1)^2 - 4(c^2 + d^2 + 1)c \cos \theta + 4c^2 + 4(c^2 + d^2) \cos^2 \theta}$$

$$F_3 = F_1 - F_2^2 + \frac{[(c^2 + d^2)^2 - 1] F_2 - 4dcF_1}{(c^2 + d^2 + 1)^2 - 4c^2}$$

$$F_4 = 2F_1F_2 - \frac{[(c^2 + d^2)^2 - 1] F_1 + 4dcF_2}{(c^2 + d^2 + 1)^2 - 4c^2}$$

These can be expanded in powers of  $d$ , with the coefficients being  $O(1)$  functions of  $l$  and  $\theta$  for  $l \rightarrow \infty$ . Thus it is found that

$$F_1 = (2 \cos \theta) d^{-1} + O(d^{-3})$$

$$F_2 = 1 + 2(1 + c \cos \theta - 2 \cos^2 \theta) d^{-2} + O(d^{-4})$$

$$F_3 = 2(4 \cos^2 \theta - 2 - c \cos \theta) d^{-2} + O(d^{-4})$$

$$F_4 = (2 \cos \theta) d^{-1} + O(d^{-3})$$

Using these, and also

$$\cos v = \left( \frac{1 - \sqrt{e}}{2} \right) \frac{1}{\sqrt{l}} [1 + O(l^{-1})], \quad \sin v = 1 + O(l^{-1})$$

then Eq. 22 and 23 yield

$$(25) \quad \pi u_{c_s} + i\pi a_s = \left( \frac{1 + \sqrt{e}}{2} \right) \frac{1}{\sqrt{l}} \int_0^\pi \cos \theta [1 + O(l^{-1})] H d\theta \\ + i \int_0^\pi [1 + O(l^{-1})] H d\theta$$

$$\begin{aligned}
 (26) \quad t_{ws} + i \frac{C_{Ls}}{2} &= \ell [1 + O(\ell^{-1})] \int_0^\pi [(\cos \nu F_3 + \sin \nu F_4) + i(\cos \nu F_4 - \sin \nu F_3)] H d\theta \\
 &= \int_0^\pi \left[ \sqrt{\ell} \left( \frac{1 + \sqrt{e}}{2} \right) \cos \theta + O(\ell^{-1/2}) \right] H d\theta \\
 &\quad + i \left( \frac{1 + \sqrt{e}}{2} \right)^2 \int_0^\pi \left[ \left( \frac{1 - \sqrt{e}}{1 + \sqrt{e}} \right) \cos \theta - 2 \cos^2 \theta + 1 + \frac{c \cos \theta}{2} + O(\ell^{-1}) \right] H d\theta
 \end{aligned}$$

Thus for  $\ell = \infty$  Eq. 25 is seen to give  $u_{cs} = 0$  and  $a_s$  in accord with Eq. 2. Also using the expansion of  $c$  from Eq. 24,

$$\frac{C_{Ls}}{2} \Big|_{\ell = \infty} = \left( \frac{1 + \sqrt{e}}{2} \right)^2 \int_0^\pi \left[ 2 \left( \frac{1 - \sqrt{e}}{1 + \sqrt{e}} \right) \cos \theta - 2 \cos^2 \theta + 1 \right] H d\theta$$

in accord with Eq. 6. Similarly one obtains

$$C_{Ds} \Big|_{\ell = \infty} = \lim_{\ell \rightarrow \infty} (2u_{cs} t_{ws}) = \frac{2}{\pi} \left( \frac{1 + \sqrt{e}}{2} \right)^2 \left( \int_0^\pi \cos \theta H d\theta \right)^2$$

in accord with Eq. 5. It can be seen that the sign of  $\sqrt{C_{Ds}}$ , important to the  $C_D$  versus  $\alpha$  variation in Eq. 4, should be taken the same as that of  $t_{ws}$  in Eq. 26, so that

$$(27) \quad \sqrt{C_{Ds}} \Big|_{\ell = \infty} = \sqrt{\frac{2}{\pi}} \left( \frac{1 + \sqrt{e}}{2} \right) \int_0^\pi \cos \theta H d\theta$$

To illustrate the characters of  $F_1, \dots, F_4$ , Fig. 7 gives their curves for  $e = 0.3$  and for  $\ell = \infty, 4, 2, 1.25$ , and  $1.1$ . Since the  $F$ 's are fairly simple functions of  $\theta$ , their values were first calculated at 10-degree intervals in  $0 \leq \theta \leq 180^\circ$  and then at intermediate values near critical points. Additional  $\theta$  values were also needed, particularly for  $\theta$  near  $\theta'$ , to sufficiently define the products  $F_1 H, \dots, F_4 H$ . Tables 5 through 9 give the 10-degree values of the  $F$ 's and of  $x(\theta)$  for  $e = 0.3, 0.4$ , and  $0.5$  and for  $\ell = \infty, 8, 4, 2.5, 2, 1.5, 1.25, 1.125$ , and  $1.1$ .

To aid in the calculation of other tables of the  $F$ 's, Tables 10 and 11 give the major parameters  $c$  and  $d$  for all the  $e$  and  $\ell$  values of the flat-plate parameter tables given later. Tables 12 and 13 give parameters  $a$  and  $b$

which enter into the wetted surface mapping relation for  $x(\theta)$  for arbitrary  $l$ ,

$$(28) \quad \sqrt{\frac{x}{l-x}} = \pm \frac{1}{b} (\cos \theta - a)$$

Table 13 gives  $bl/N^2$  that is used in obtaining  $t_{ws} + iC_{Ls}/2$  since

$$\frac{bl}{N} e^{-i\nu} = \frac{bl}{N^2} [(c-a) - i(d-b)]$$

Typical steps in the treatment of the NACA 0010 thickness distribution and the uniform-load camber line are described below.

#### NACA 0010 THICKNESS DISTRIBUTION

The first step in treating a profile with a round leading edge is the removal of the leading-edge singularity in  $H(\theta)$ . As discussed in Ref. 1, this is done by subtracting the appropriate point-drag profile. From Eq. 12 of this report, it can be seen that the singular term in the 0010 profile's  $H(x)$  is  $\pm \delta_{-\frac{1}{2}} x^{-\frac{1}{2}}$  with  $\delta_{-\frac{1}{2}} = 0.074225$ . From the open-model point-drag profile expression in Ref. 1, the corresponding slope distribution  $\tilde{H}(x)$  for arbitrary  $l$  is

$$(29) \quad \tilde{H}(x) = \pm \tilde{u}_c \sqrt{\frac{l}{x}} \sqrt{1 - \frac{x}{l}}$$

Thus for the 0010 profile,  $\tilde{u}_c = 0.074225/\sqrt{l}$  and  $H$  in the  $s$ -parameter integrals is replaced by

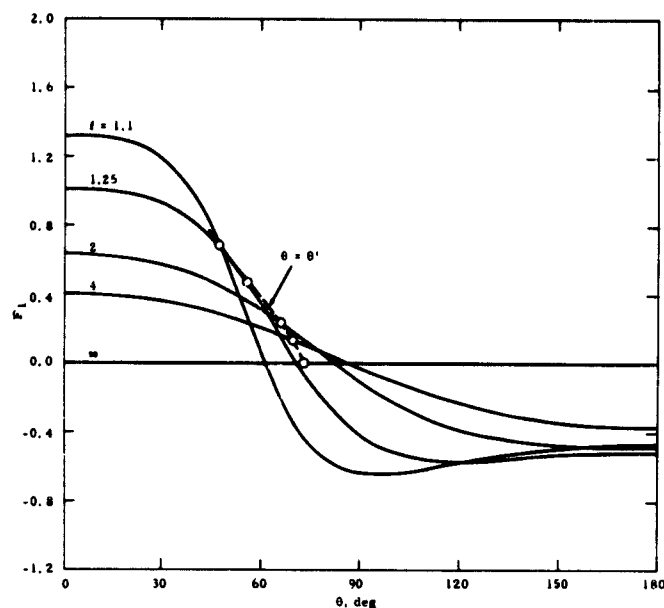
$$\bar{H} = H - \tilde{H} = \pm \left[ \delta_{-\frac{1}{2}} x^{-\frac{1}{2}} \left( 1 - \sqrt{1 - \frac{x}{l}} \right) + \delta_0 + \delta_1 x + \delta_2 x^2 + \delta_3 x^3 \right]$$

Figure 8 show  $|\bar{H}|$  versus  $x$  for several  $l$  values. Note that  $\bar{H} = \pm \delta_0$  at  $x = 0$ , so that  $\bar{H}(\theta)$  will be discontinuous at  $\theta = \theta'$ . As an example of the corresponding  $\bar{H}(\theta)$ , Fig. 9 gives  $\bar{H}(\theta)$  for  $e = 0.3$  and  $l = 4$ . For the same  $e$  and  $l$ , Fig. 10 gives the corresponding curves of  $F_1 \bar{H}$ , ...  $F_4 \bar{H}$  and the planimeter-determined areas.

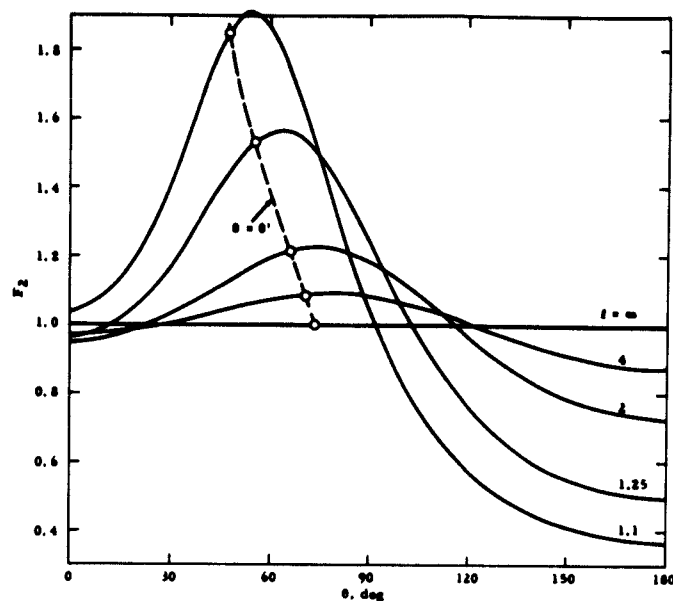
When the resultant  $s$ -parameter values are identified by bars and the point-drag contributions by tildes, the final  $s$ -parameters are obtained using

$$(30) \quad \begin{aligned} u_{cs} &= \bar{u}_{cs} + \tilde{u}_{cs}, & a_s &= \bar{a}_s + \tilde{a}_s = a_s \\ t_{ws} &= \bar{t}_{ws} + \tilde{t}_{ws} = \bar{t}_{ws} + \pi \tilde{u}_c l, & C_{Ls} &= \bar{C}_{Ls} + \tilde{C}_{Ls} = \bar{C}_{Ls} \end{aligned}$$

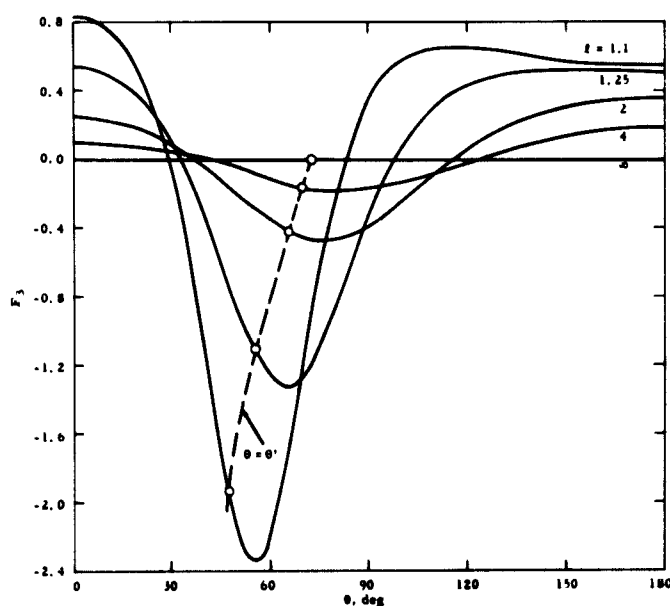




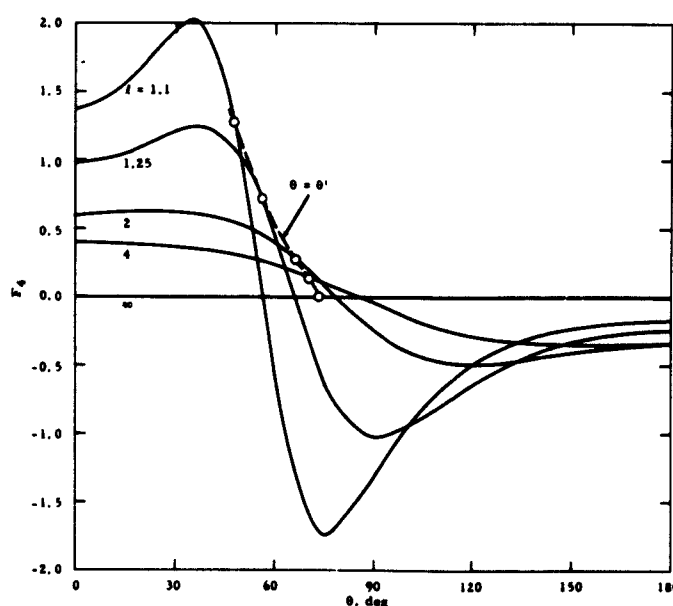
(a)  $F_1$



(b)  $F_2$



(c)  $F_3$



(d)  $F_4$

FIG. 7. Integrand Factors in s-Parameter Integrals,  $e = 0.3$  for Various  $l$  Values.

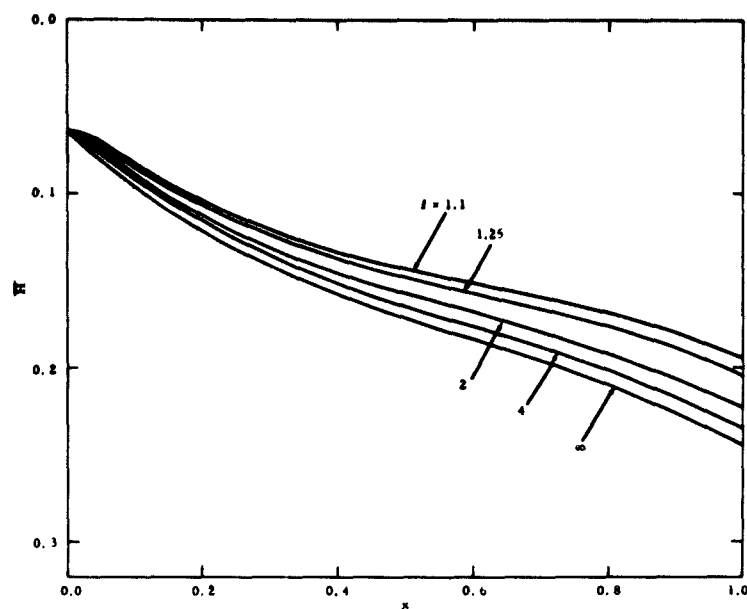


FIG. 8.  $\bar{H}(x)$  for NACA 0010 Profile for Various  $l$  Values.

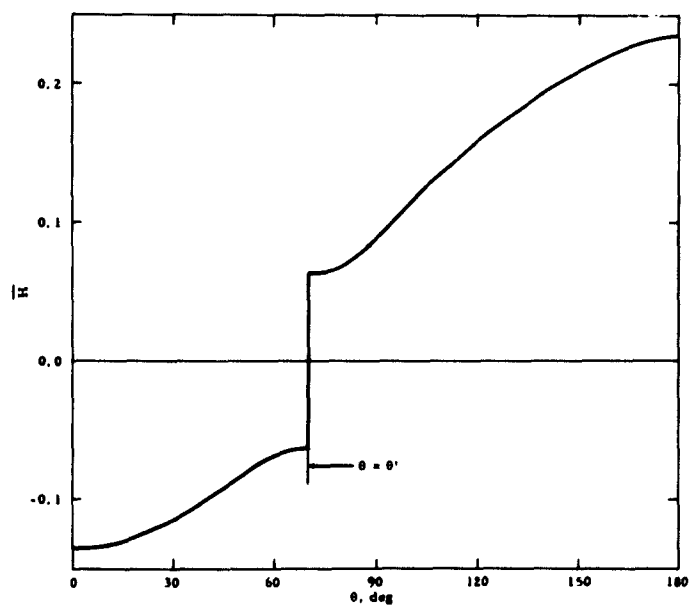
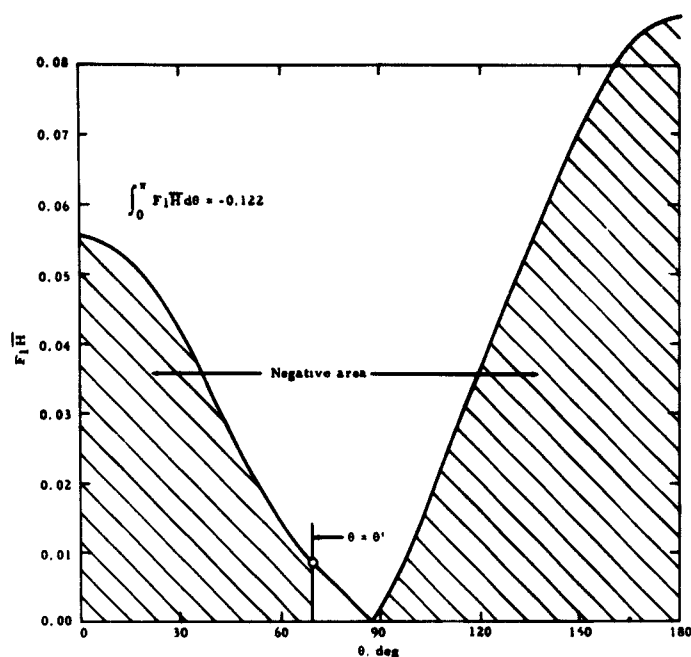
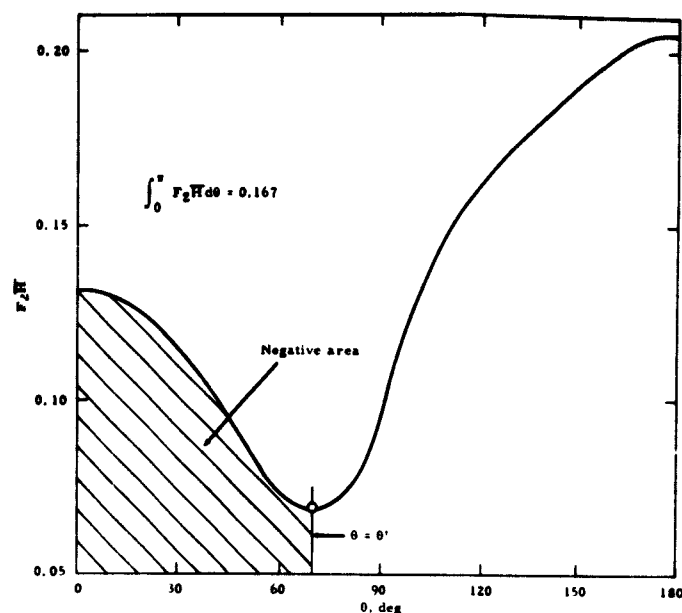


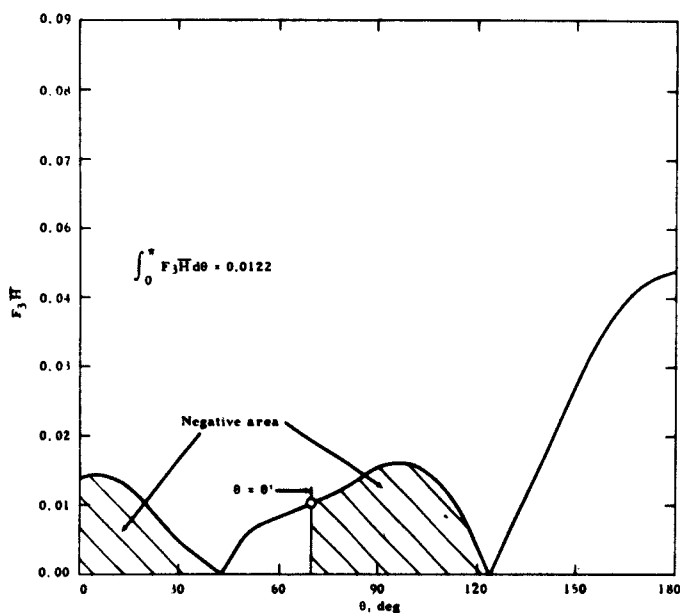
FIG. 9.  $\bar{H}(\theta)$  for NACA 0010 Profile,  $e = 0.3$  and  $l = 4$ .



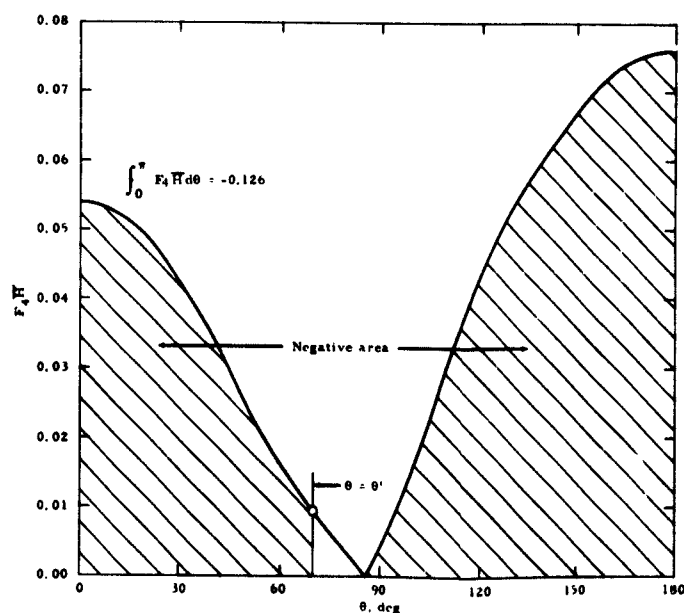
(a)  $F_1 H$



(b)  $F_2 H$



(c)  $F_3 H$



(d)  $F_4 H$

FIG. 10. s-Parameter Integrands for the  $\bar{H}(\theta)$  of the NACA 0010 Profile,  $e = 0.3$  and  $l = 4$ .

Figures 11 and 12 give the curves of the  $s$ -parameters corresponding to  $\tilde{H}$  and  $H$ , showing how important are the tilde contributions to  $u_{cs}$  and  $t_{ws}$ .  $\tilde{C}_{Ds}$  and  $\tilde{C}_{Ls}$  have been evaluated for  $l = \infty$  using Eq. 27 to check continuity with the values for finite  $l$ .

One check on the accuracy of the calculations can be made as follows. For  $e = 0.3$  and  $l = \infty$ , the analytically determined values for the 0010 profile, from Fig. 2, are

$$\sqrt{C_D^0} = -0.0059, \quad C_L^0 = -0.306$$

The planimeter results are

$$a_s = 0.0414, \quad C_{Ds} = (0.0161)^2, \quad C_{Ls} = -0.163$$

which imply

$$\sqrt{C_D^0} = \sqrt{C_{Ds}} - \sqrt{2\pi} a_s \left( \frac{1 - \sqrt{e}}{2} \right) = -0.0068$$

$$C_L^0 = C_{Ls} - 2\pi a_s \left( \frac{1 + \sqrt{e}}{2} \right)^2 = -0.319$$

The effect of the errors in  $\sqrt{C_D^0}$  and  $C_L^0$  can be seen to be small, as follows.  $C_D$  and  $C_L$  from Eq. 8 can be put in the forms

$$C_D = 2\pi (a - a^+)^2 \left( \frac{1 - \sqrt{e}}{2} \right)^2, \quad a^+ = \frac{-\sqrt{C_D^0}}{\sqrt{2\pi} \left( \frac{1 - \sqrt{e}}{2} \right)}$$

$$C_L = 2\pi (a - a|_0)^2 \left( \frac{1 + \sqrt{e}}{2} \right)^2, \quad a|_0 = \frac{-C_L^0}{2\pi \left( \frac{1 + \sqrt{e}}{2} \right)^2}$$

where  $a|_0$  is  $a$  for  $C_L = 0$ . Thus  $a^+$  is in error by about +0.09 degree and  $a|_0$  by about +0.18 degree. Thus the error due to the planimeter calculation inaccuracy will be small away from the zero drag and zero lift angles.

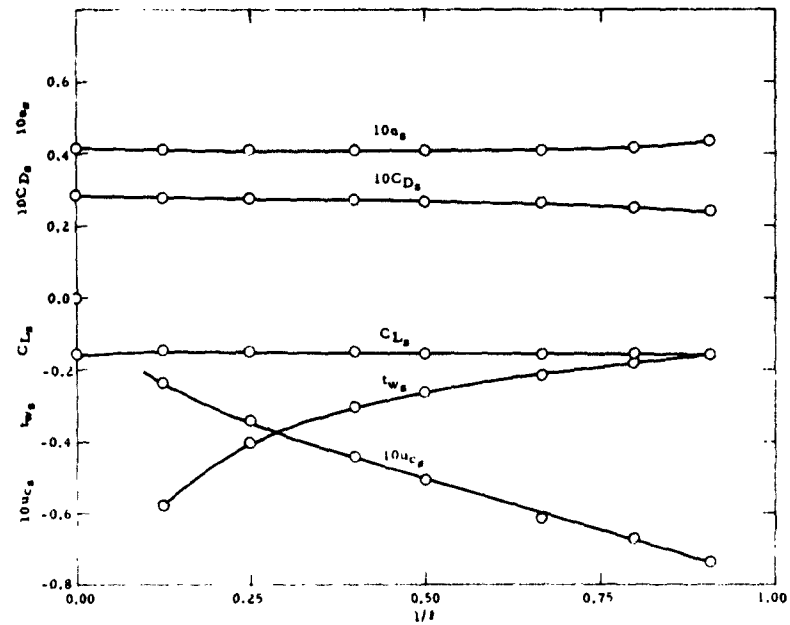


FIG. 11. Planimeter Results for the s-Parameters Versus  $1/l$  for  $H(0)$  of the NACA 0010 Profile,  $e = 0.3$ .

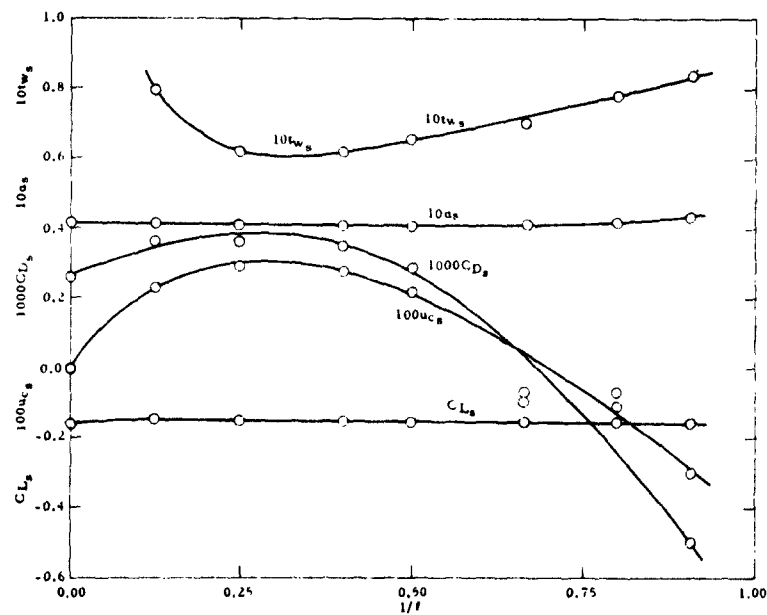


FIG. 12. Final s-Parameters Versus  $1/l$  for the NACA 0010 Profile,  $e = 0.3$ .

## UNIFORM-LOAD CAMBER LINE

The uniform-load camber line has slope singularities at the leading and trailing edges. For the planimeter calculations, the singularities were eliminated in a practical and realistic way by making  $H(x)$  uniform in the intervals  $0 \leq x < 0.005$  and  $0.995 < x \leq 1$ , and by choosing the  $H$  values therein to match the exact profile contour height at the interval end points. Since  $H(x)$  is antisymmetrical about  $x = 0.5$ , Fig. 13 gives the approximating  $H(x)$  only for  $0 \leq x \leq 0.5$ . Note that for  $e = 0.3$  the discontinuity at  $x = 0.005$  in Fig. 13 will appear at three  $\theta$  values in the  $s$ -parameter integrands, corresponding to  $x = 0.005$ ,  $y = 0\pm$ , and  $x = 0.995$ ,  $y = 0-$ . Figure 14 gives the resultant curve of  $H(\theta)$  for  $e = 0.3$ ,  $l = 4$ . There is no sign reversal at  $\theta = \theta'$  for a camber line. Figure 15 gives the resultant curves of  $F_1H, \dots, F_4H$  and the corresponding areas, which lead to the  $s$ -parameter values for  $l/l = 1/4$  seen in the final curves in Fig. 16.

In order to check the combined accuracy of the  $H$  approximation and the planimeter integration, the results for  $l = \infty$  are again compared. The accurate machine computations for  $e = 0.3$  shown in Fig. 3 and 4 give

$$\sqrt{C_D^0} = 0.142, \quad C_L^0 = 0.324$$

The planimeter results for  $l = \infty$  are

$$\alpha_s = 0.0799, \quad \sqrt{C_{D_s}} = 0.1815, \quad C_{L_s} = 0.634$$

and these lead to

$$\sqrt{C_D^0} = 0.136, \quad C_L^0 = 0.333$$

Proceeding as for the 0010 profile, it is found that the  $\alpha^+$  error is about +0.66 degree and that of  $\alpha$  for  $C_L = 0$  is about -0.14 degree.

While the accuracy of the planimeter integrations has been shown in two cases for  $l = \infty$ , it is necessary also to check on the integrals and the planimeter calculation accuracy for finite  $l$ . This has been done in Appendix B by considering the vented wedge and comparing its  $s$ -parameter values from planimeter integration with those from the formal solution constructed of point singularities on the unit circle.

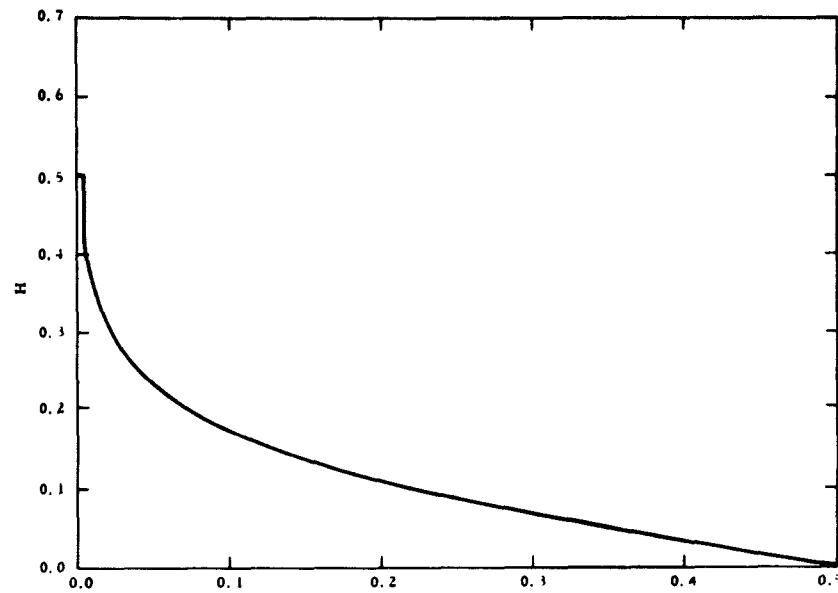


FIG. 13.  $H(x)$  for Uniform-Load Camber Line With Edge Approximation.

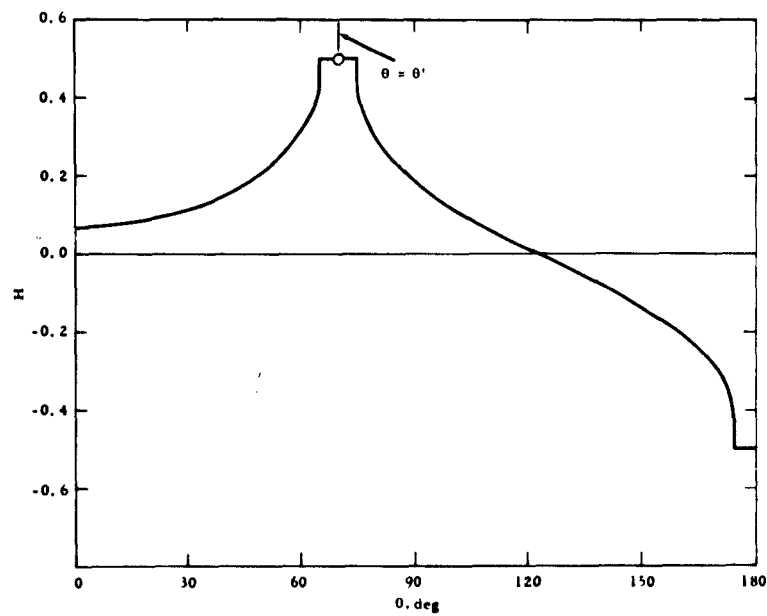


FIG. 14.  $H(\theta)$  for Uniform-Load Camber Line,  $e = 0.3$  and  $l = 4$ .

## THE FLAT-PLATE PARAMETERS

## OPEN MODEL

As shown in Ref. 1, the open-model flat-plate solution  $P(\zeta)$  leads to the key parameters for unit angle of attack:

$$(31) \quad \begin{aligned} u_{cP} &= \beta_P \left( \frac{a}{b} - \frac{\cos \lambda}{b\Lambda} \right), \quad \frac{1}{\beta_P} = 1 + \frac{\sin \lambda}{b\Lambda} \\ t_{wP} &= \frac{\pi \beta_P l}{bN} \left[ -(1 - a^2) \cos \nu + ab \sin \nu \right] \\ C_{LP} &= \frac{2\pi \beta_P l}{bN} \left[ ab \cos \nu + (1 - a^2) \sin \nu \right] \end{aligned}$$

Tables 15, 16, and 17 give  $u_{cP}$ ,  $t_{wP}$ , and  $C_{LP}$  respectively for 15 values of  $l$ :

$\infty, 32, 16, 12, 8, 4, 3, 2.5, 2, 1.75, 1.5, 1.25, 1.125, 1.1, 1.0$

and 13 values of  $e$ :

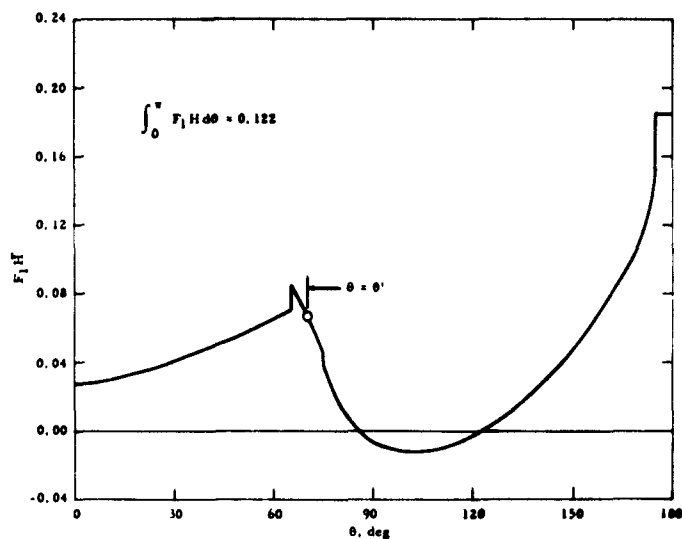
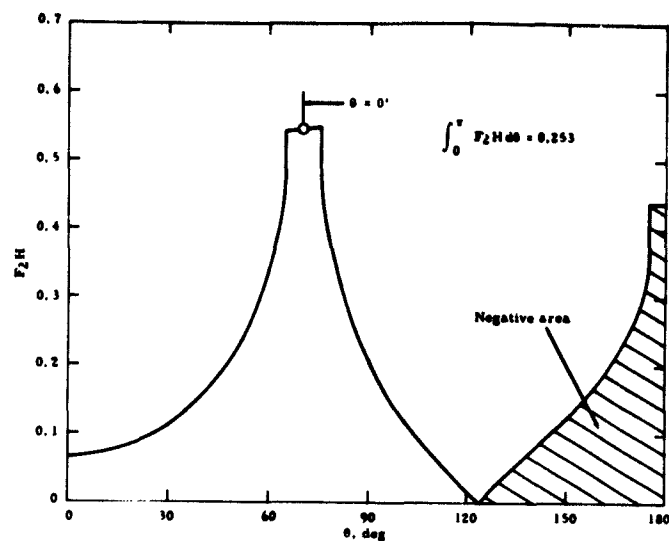
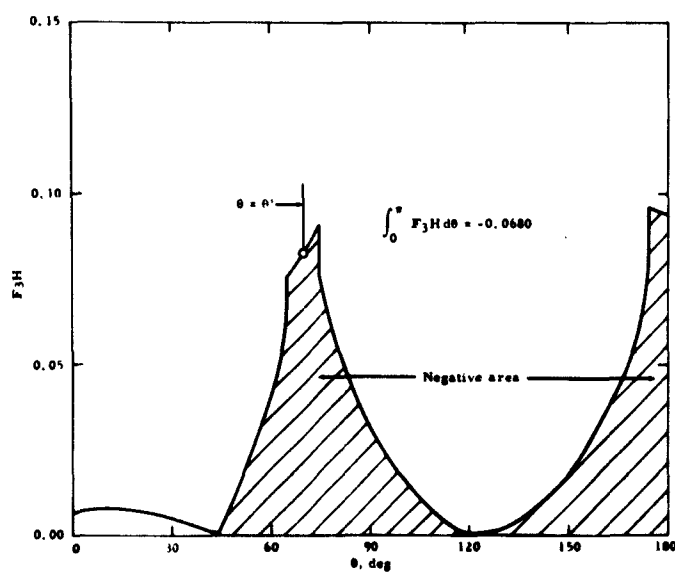
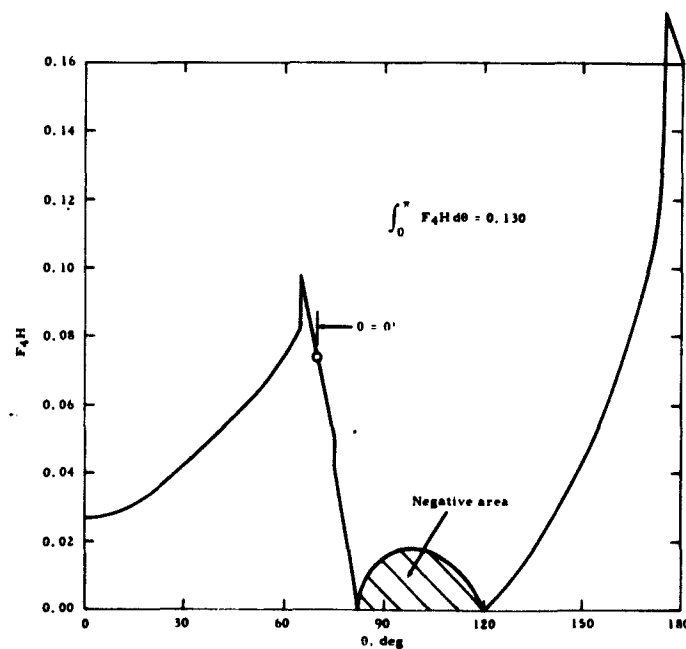
$0, 0.025, 0.05, 0.1, 0.2, 0.3, \dots 1.0$

The boundary cases are

Case	$u_{cP}$	$t_{wP}$	$C_{LP}$
$l = \infty$	0	$\infty$	$2\pi \left( \frac{1 + \sqrt{e}}{2} \right)^2$
$l = 1$	$\left( \frac{1 - \sqrt{e}}{1 + \sqrt{e}} \right)^{1/2}$	$\pi \left( \frac{1 - \sqrt{e}}{2} \right)^{3/2} \left( \frac{1 + \sqrt{e}}{2} \right)^{1/2}$	$\frac{1 + \sqrt{e}}{2}$
$e = 0$	$\sqrt{l} - \sqrt{l-1}$	$\frac{\pi}{2} \sqrt{l}$	$\pi \sqrt{l} (\sqrt{l} - \sqrt{l-1})$
$e = 1$	0	0	$2\pi$

For each case but the first,  $C_{DP} = 2u_{cP}t_{wP}$ , and for  $l = \infty$ ,



(a)  $F_1 H$ (b)  $F_2 H$ (c)  $F_3 H$ (d)  $F_4 H$ FIG. 15.  $s$ -Parameter Integrands for  $H(\theta)$  of Uniform-Load Camber Line,  $e = 0.3$  and  $l = 4$ .

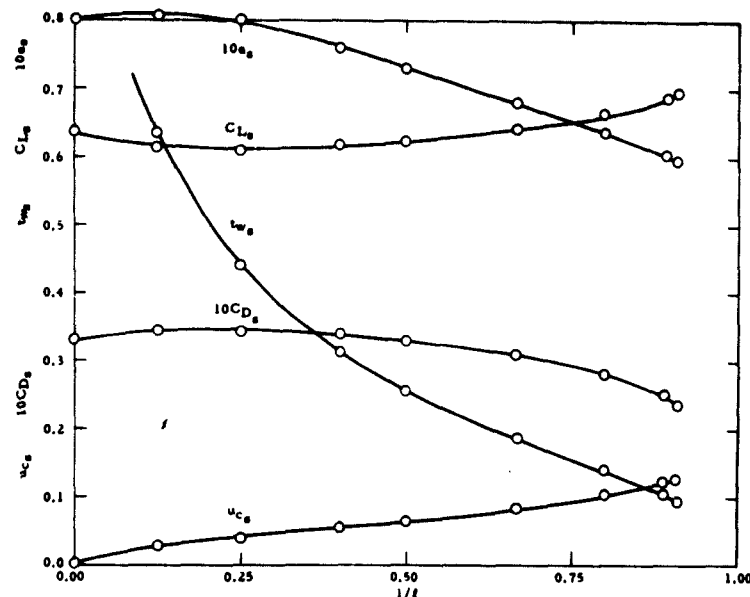


FIG. 16. Planimeter Results for s-Parameters Versus  $1/l$  for Uniform-Load Camber Line,  $e = 0.3$

$$C_{DP} = \lim_{l \rightarrow \infty} \left( 2u_{cP} t_{wP} \right) = 2\pi \left( \frac{1 - \sqrt{e}}{2} \right)^2$$

In the last case,  $e = 1$ , the solutions for all  $l$  have collapsed to the solution for fully wetted flow.

#### CLOSED MODEL

The key parameters of the closed-model, flat-plate solution  $Q(\zeta)$ , also for unit angle of attack, are given in Ref. 1 as

$$u_{cQ} = \beta_Q \left[ \frac{u_{cP}}{\beta_P} + C' \left( \Lambda + \frac{1}{\Lambda} \right) \sin \lambda \right], \quad \frac{1}{\beta_Q} = \frac{1}{\beta_P} - C' \left( \Lambda - \frac{1}{\Lambda} \right)$$

$$(32) \quad C_{DQ} = 2\pi C_Z^2 = 8\pi (bC'\beta_Q)^2 l,$$

$$C_{LQ} = \frac{\beta_Q}{\beta_P} C_{LP} - \beta_Q C' \left[ \sin(\lambda - \nu) - \frac{1}{\Lambda^2} \sin(\lambda + \nu) \right] \frac{b\Lambda}{2N}$$

where the closure condition gives

$$(33) \quad C' \left[ \cos(\lambda - \nu) + \frac{1}{\Lambda^2} \cos(\lambda + \nu) \right] = t_{WP} \left( \frac{bN}{\pi \beta_P l} \right) \frac{1}{b^2 \Lambda}$$

Tables 18, 19, and 20 give  $u_{cQ}$ ,  $C_{DQ}$ , and  $C_{LQ}$  for the same  $e$  and  $l$  values as the P-parameters.

For two of the four boundary cases, the closed and open models are identical, because the closure singularity is unimportant for  $l = \infty$  and is zero for  $e = 1$ . For  $l \rightarrow 1$ , the closure singularity increases without limit and  $u_{cQ}$  and  $C_{LQ} \rightarrow \infty$ . The  $C_{DQ}$  behavior for  $l \rightarrow 1$  is more complicated, with  $C_{DQ} \rightarrow \infty$  for  $e = 0$ , and  $C_{DQ} \rightarrow 0$  for  $e > 0$  due to the leading-edge singularity. For  $e = 0$ , the closed model has

$$u_{cQ} = \frac{1}{\sqrt{l-1}}, \quad C_{DQ} = C_{LQ} = \frac{\pi l}{\sqrt{l-1}} (\sqrt{l} - \sqrt{l-1})$$

The general character of these P- and Q-parameters as functions of  $e$  and  $l$  can be seen in Fig. 6 and 7 of Ref. 1, where they are presented in terms of the flat plate's hydrodynamic coefficients for the two models, using

$$C_{D_0}/a^2 = C_{DP}, \quad C_{D_{cl}}/a^2 = C_{DQ}, \quad C_{L_0}/a = C_{LP}, \quad \text{and} \quad C_{L_{cl}}/a = C_{LQ}.$$

#### DISCUSSION

It is interesting to see the character of the differences between the force coefficients for the two models, by comparing their forms for  $e = 0$ . The open-model relations for  $e = 0$  given above lead to

$$\frac{C_D}{a^2} = \frac{C_L}{a} = \frac{\pi}{2} \left[ 1 + \left( \frac{K}{2a} \right)^2 \right]$$

while the corresponding closed-model relations produce

$$\frac{C_D}{a^2} = \frac{C_L}{a} = \frac{\pi}{2} \left[ 1 + \left( \frac{K}{2a} \right)^2 \right] \left[ 2 \left( \frac{2a}{K} \right)^2 \sqrt{1 + \left( \frac{K}{2a} \right)^2} - 1 \right]$$

Thus the closed model for  $e = 0$  and  $K/2a \rightarrow 0$  has

$$\frac{C_D}{a^2} = \frac{C_L}{a} = \frac{\pi}{2} \left[ 1 + \frac{3}{4} \left( \frac{K}{2a} \right)^2 + O \left( \frac{K}{2a} \right)^4 \right]$$

In contrast to these results for free-stream speed linearization, the well-known cavity-wall-speed linearization always gives linear variation with  $K$  (not  $K/a$ ) of the hydrodynamic coefficients for  $K \rightarrow 0$ . The conversion from the free-stream-speed linearization to the other is quite simple, as discussed in Appendix A of Ref. 3. It is easy to see that the  $C_D$  conversion given there for  $e = 1$  applies for all  $e$  and for both the closed and open models. Thus for a given profile, cavity length, and particular cavity termination within the open, partly closed, and closed model family,

$$(34) \quad C_{D_{cw}} = (1 + K_{cw}) C_{D_{fs}}, \quad C_{L_{cw}} = (1 + K_{cw}) C_{L_{fs}}, \quad C_{M_{cw}} = (1 + K_{cw}) C_{M_{fs}}$$

where

$$(35) \quad 1 - \frac{1}{\sqrt{1 + K_{cw}}} = \frac{K_{fs}}{2}$$

Thus, for example, for the vented flat plate with  $e = 0$ , the closed-model result is

$$\frac{C_{D_{cw}}}{a^2} = \frac{C_{L_{cw}}}{a} = \pi(1 + K_{cw}) \frac{l}{\sqrt{l-1}} (\sqrt{l} - \sqrt{l-1}), \quad 1 - \frac{1}{\sqrt{1 + K_{cw}}} = \frac{1}{\sqrt{l-1}}$$

Figure 17 shows that the consequent differences in the curves of  $C_D/a^2$  and  $C_L/a$  versus  $K$  are not important for the small angles of attack typical of vented hydrofoil applications.

Applications of the six flat-plate parameters are illustrated next by generation of the  $C_D$  and  $C_L$  versus  $K$  curves for two hydrofoil profiles that have been tested in fully vented flow (Ref. 5). As discussed in Ref. 1, the P-parameters are used in two ways: (1) to shift from the open-model, smooth-entry condition to the cusp-closure condition, and (2) to obtain the open-model results for arbitrary attack angle of an arbitrary profile, starting with its cusp-closure parameters. The Q-parameters are used to obtain the closed-model results for arbitrary attack angle of an arbitrary profile, starting with its cusp-closure parameters.

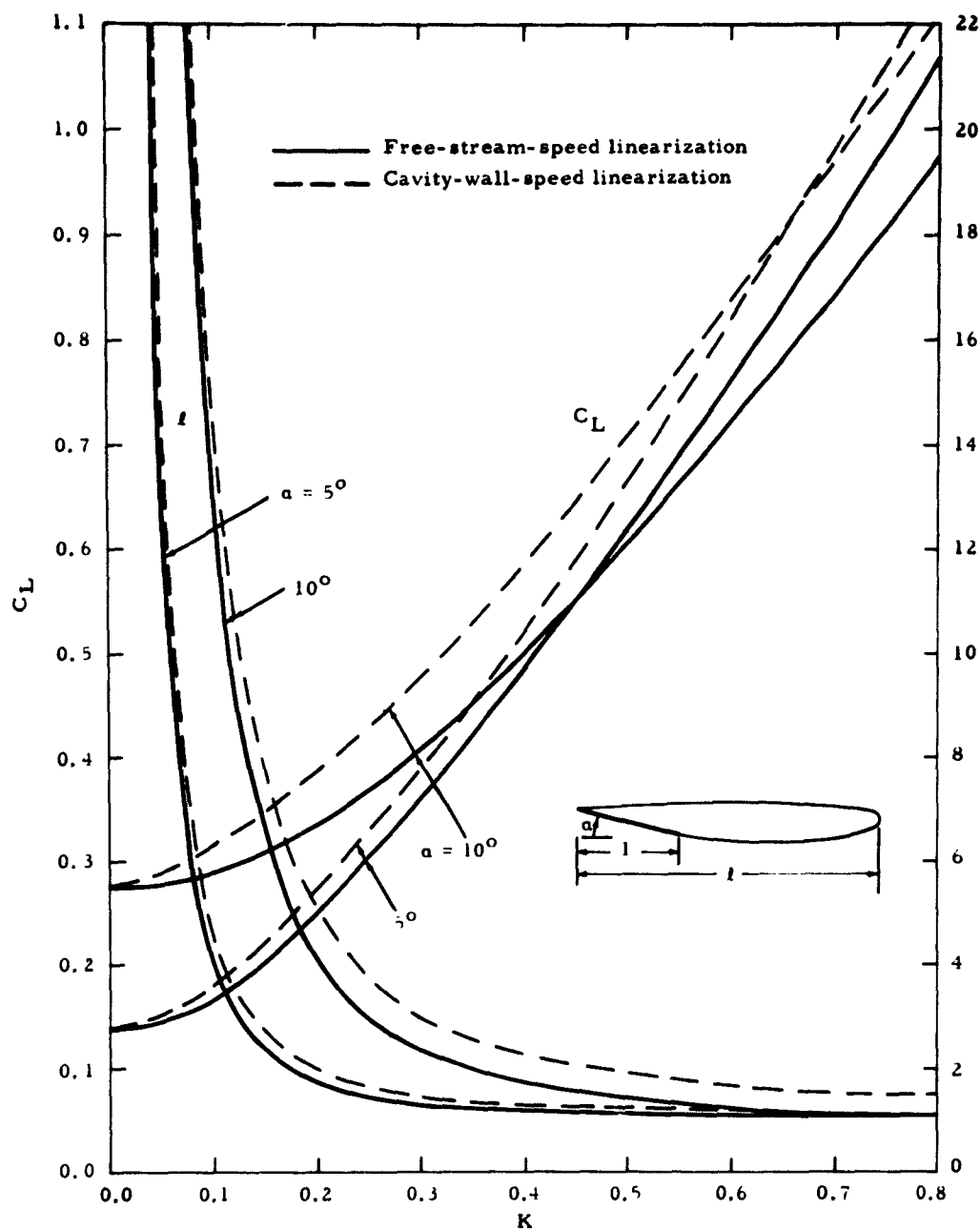


FIG. 17. Comparison of Lift Coefficient and Cavity Length Versus Cavity Number for Vented Flat Plate,  $e = 0$  and Closed Model, According to Free-Stream-Speed and Cavity-Wall-Speed Linearization.

# EXAMPLES OF THEORETICAL $C_L$ AND $C_D$ VERSUS $K$ AND TWO COMPARISONS OF THEORY AND EXPERIMENT

## HYDROFOIL A

The profile of Hydrofoil A has the NACA 0010 thickness distribution and the uniform-load camber line for design  $C_L$  of 0.2. Thus the  $s$ -parameters for Hydrofoil A,  $e = 0.3$ , are simply obtained from previous results, using, in obvious notation,

$$u_{cs} = \left( u_{cs} \right)_{0010} + 0.2 \left( u_{cs} \right)_{a=1.0}$$

and corresponding forms for  $a_s$ ,  $t_{ws}$ , and  $C_{Ls}$ . All other combinations of the NACA four-digit thickness distribution and the uniform-load camber line for  $e = 0.3$  can also be considered with the theoretical results in this report because the thickness and camber distributions were treated separately. If Hydrofoil A had been treated from the start, only other thickness ratios each for design  $C_L$  of twice the thickness ratio could be considered.

As discussed in Ref. 1, the cusp-closure angle of attack,  $\alpha^+$ , is a natural and convenient reference angle for each cavity length. The values of  $\alpha^+$ ,  $u_c^+$  and  $C_L^+$  are obtained by combining the P solution and the particular profile's  $s$ -solution for each  $l$  to make  $t_w = 0$ . Figure 18

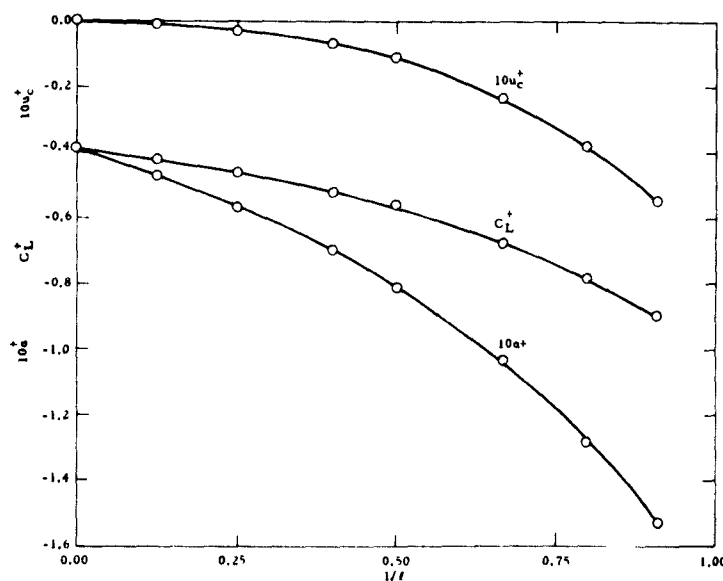


FIG. 18. Cusp-Closure Parameters for Hydrofoil A,  $e = 0.3$ .

gives the cusp-closure parameters for Hydrofoil A,  $e = 0.3$ , obtained with

$$0 = t_{ws} + (a^+ - a_s)t_{wp}$$

$$u_c^+ = u_{cs} - \frac{t_{ws}}{t_{wp}} u_{cp}, \quad C_L^+ = C_{Ls} - \frac{t_{ws}}{t_{wp}} C_{LP}$$

Having  $K^+ = 2u_c^+$  and  $a^+$  for each  $l$ , then as discussed in Ref. 1, all  $a$  values for  $a \geq a^+$  correspond to proper cavity solutions in the restricted sense that the closure singularity has proper sign. This merely means that cases of definite free-streamline crossing have been eliminated, and of course it is likely that experimental cavity conditions will not extend down to the negative  $K$  region typically included in the proper solution domain, as seen below. A more detailed discussion of solution domains is given in Appendix B.

The proper solution domains for Hydrofoil A,  $e = 0.3$  for  $\infty \leq l \leq 1.1$ , are given in Fig. 19a and b for the open and closed models, respectively. The vertical bars give typical experimental  $K$  values for what was labeled fully vented flow in the water-tunnel tests (Ref. 5). Since the corresponding cavities extended out of view or were at least two or chord lengths long, there is a first indication of conflict between the theory here for unbounded flow and the tunnel experiments, because the theoretical cavity lengths for the experimental  $K$  and  $a$  values are typically less than 1.5 chord lengths.

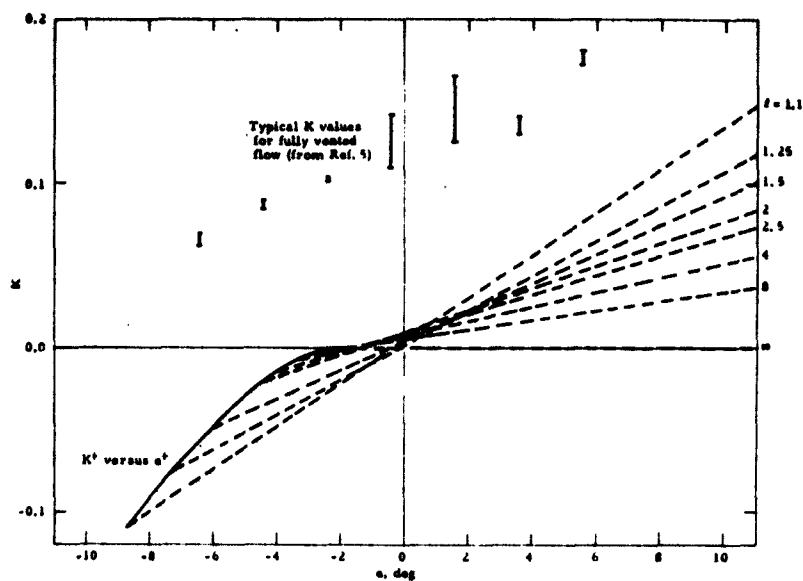
Since the open-model  $K$ ,  $a$  range is farther from the experimental conditions, only the closed model is considered in the following detailed presentation of theoretical results and comparison with experiment. However, the open-model curves essentially coincide with the closed-model curves but terminate at very low  $K$  values.

As discussed in Ref. 1, simple combinations of the cusp-closure parameters and the  $Q$ -parameters lead to the closed model  $C_L$ ,  $C_D$ , and  $K$  versus  $l$  and  $a$ . Thus Fig. 20 and 21 present the curves (solid lines) of  $C_D$  and  $C_L$  versus  $K$  for various constant  $a$  values for Hydrofoil A,  $e = 0.3$ . The dashed straight lines in Fig. 21 are the contours of constant  $l$ .

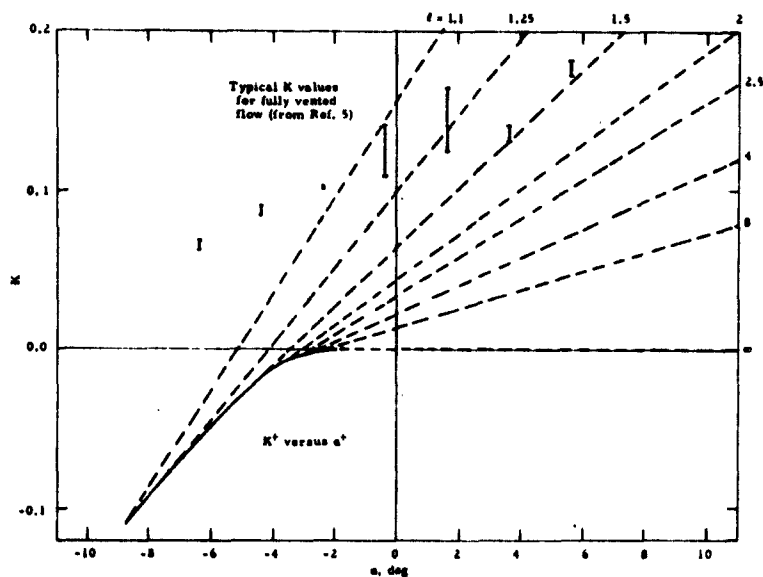
The underlying simplicity of the structure of Fig. 21 is noteworthy. For each  $l$ , as  $a$  increases from  $a^+$ , one moves toward higher  $C_L$  and  $K$  along a straight line since

$$C_L = C_L^+ + (a - a^+)C_{LQ}, \quad K = K^+ + 2(a - a^+)u_{cQ}$$

Also equally spaced  $a$  values appear at equal intervals along each constant  $l$  line, the interval depending on  $l$ . The  $l$  contour curves have



(a) Open model



(b) Closed model

FIG. 19.  $K$ ,  $\alpha$  Domain of Proper Full-Cavity Solutions for Hydrofoil A,  $e = 0.3$ , and Comparison With Experimental Test Conditions.



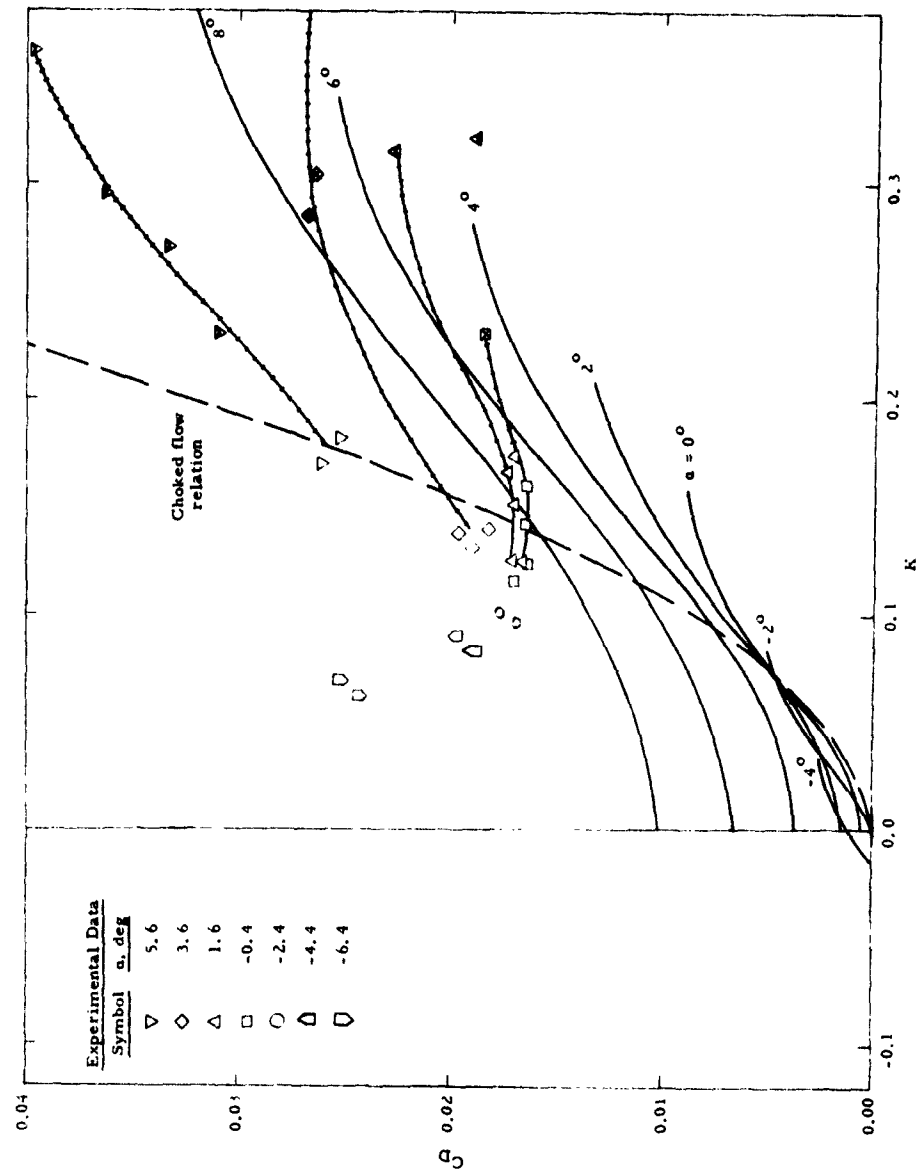


FIG. 20. Theoretical  $C_D$  Versus  $K$  for Hydrofoil A,  $e = 0.3$ , for Various  $\alpha$  Values, and Comparison With Experiment. Closed model.

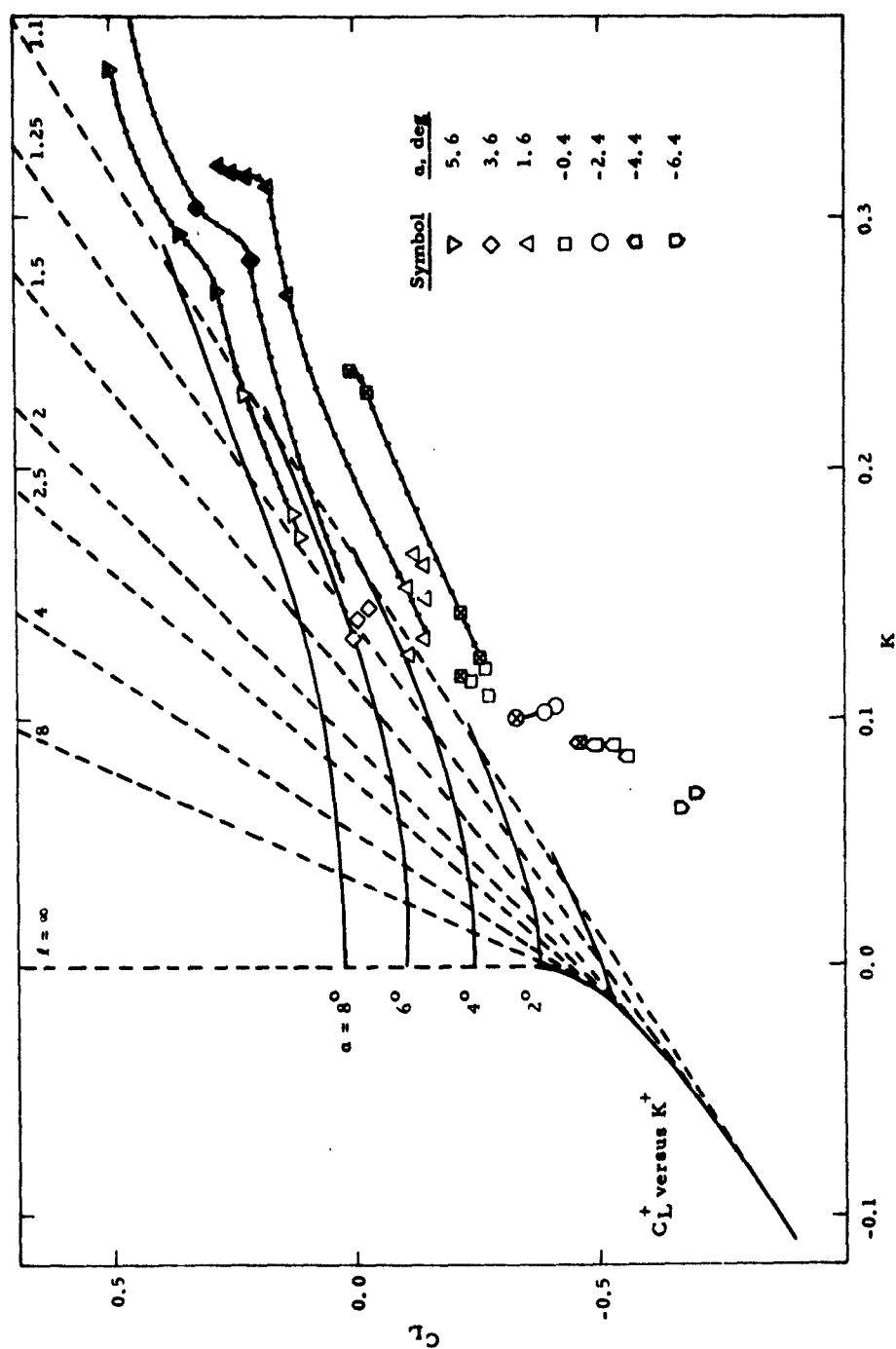


FIG. 21. Theoretical  $C_L$  Versus  $K$  for Hydrofoil A,  $e = 0.3$ , for Various  $\alpha$  Values, and Comparison With Experiment. Closed model.

been omitted from Fig. 20 to avoid crowding, but it can be seen that these would have parabolic shape, and if  $\sqrt{C_D}$  were plotted versus  $K$ , the  $l$  contours would be straight lines.

However, greater insight into the complicated structure of Fig. 20 can be obtained more easily by plotting  $\sqrt{C_D}$  versus  $\alpha$  as in Fig. 22. The  $l$  contours are again straight lines and the intersections with the  $K$  contours are spaced along each  $l$  contour at intervals proportional to the  $K$  increments. Note that there are two contours for  $K = 0$  in the proper solution domain ( $\sqrt{C_D} \geq 0$ ). The first is that for  $l = \infty$ , with  $\alpha \geq \alpha^+$ . The second, for finite  $l$ , is similar to the type of solution for finite  $l$  and  $K = 0$  which was discussed in Appendix B of Ref. 2. Since the defining equation is

$$K = 0 = 2 \left[ u_c^+ + (\alpha - \alpha^+) u_{cQ} \right]$$

so that

$$\sqrt{C_D} = (\alpha - \alpha^+) \sqrt{C_{DQ}} = -(u_c^+/u_{cQ}) \sqrt{C_{DQ}}$$

the intersection of the two contours is at  $l = \infty$  and

$$\sqrt{C_D} = \sqrt{2\pi} \left( \frac{1 - \sqrt{e}}{2} \right) \left[ \lim_{l \rightarrow \infty} (-u_c^+/u_{cQ}) \right]$$

This intersection has been estimated by extrapolation in Fig. 22.

The various types of experimental data points in Fig. 20 and 21 and the choked-flow curve in Fig. 20 are discussed later.

## HYDROFOIL B

Because this modified NACA 652-015 profile is uncambered, the theoretical treatment for Hydrofoil B,  $e = 0.3$  is similar to that for the NACA 0010 profile. Thus only the final closed-model curves of  $C_D$  and  $C_L$  versus  $K$  and  $\alpha$  are given in Fig. 23 and 24, along with the corresponding experimental fully vented data from Ref. 5.

## DISCUSSION

The agreement between theory and experiment seen in Fig. 20 to 24 is poorer than has been found in previous cases of both cavitating profiles for  $e = 0, 0.5$ , and  $1.0$  and of vented profiles for  $e = 0$  and  $1$ . It is believed that any major errors in the theoretical calculations would have been detected by the various checks described earlier. While the accuracy of the planimeter integrations decreases for small  $l$  due to the greater complexity of  $F_1, \dots, F_4$ , the major causes of the differences between the theory for unbounded flow and the experiments are thought to be real-fluid and tunnel blockage effects, as discussed below.

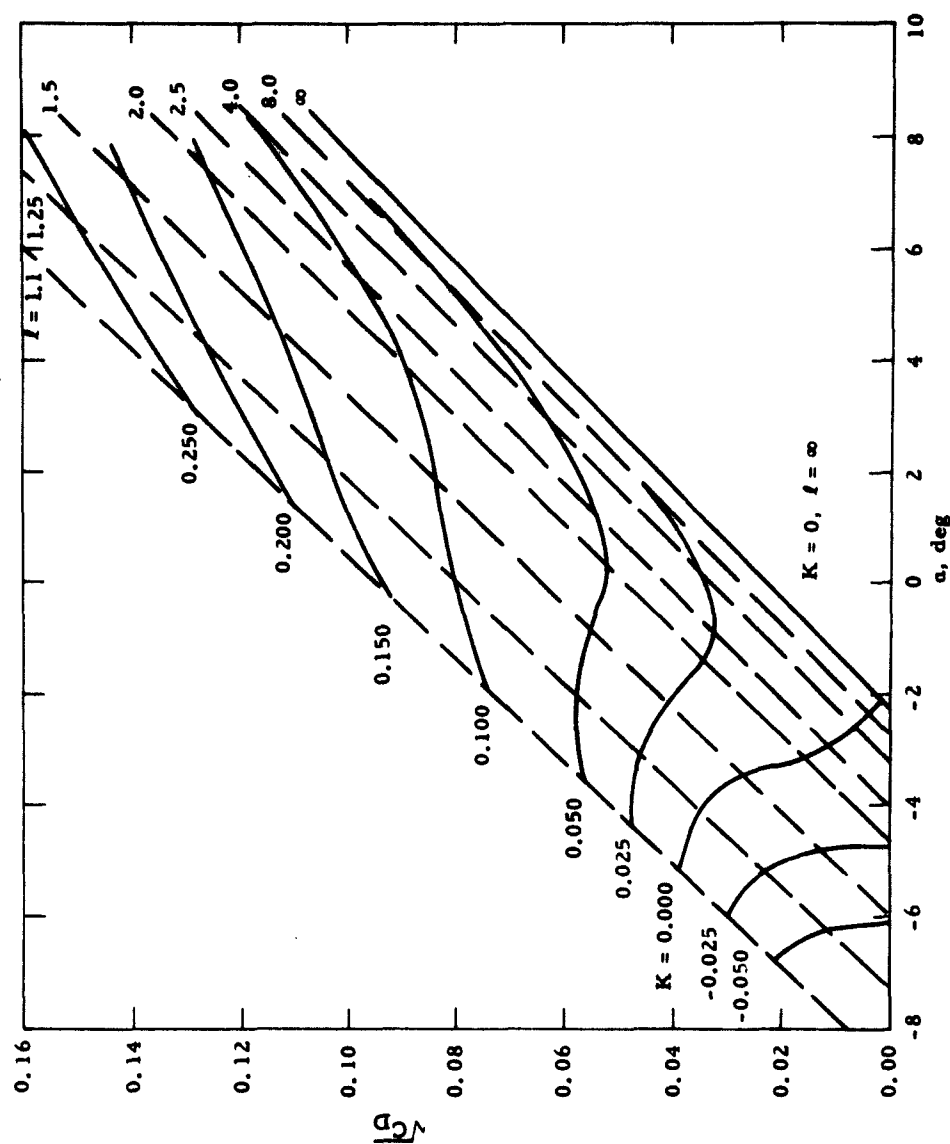


FIG. 22. Theoretical  $\sqrt{C_D}$  Versus  $\alpha$  for Hydrofoil A,  $e = 0.3$ , for Various  $K$  Values. Closed model.

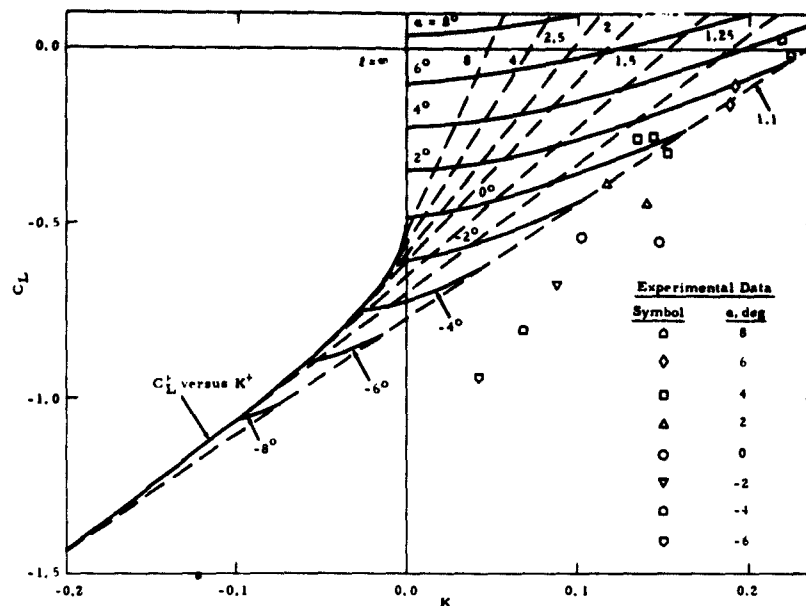


FIG. 23. Theoretical  $C_L$  Versus  $K$  for Hydrofoil B,  $e = 0.3$ , for Various  $\alpha$  Values, and Comparison With Experiment. Closed model.

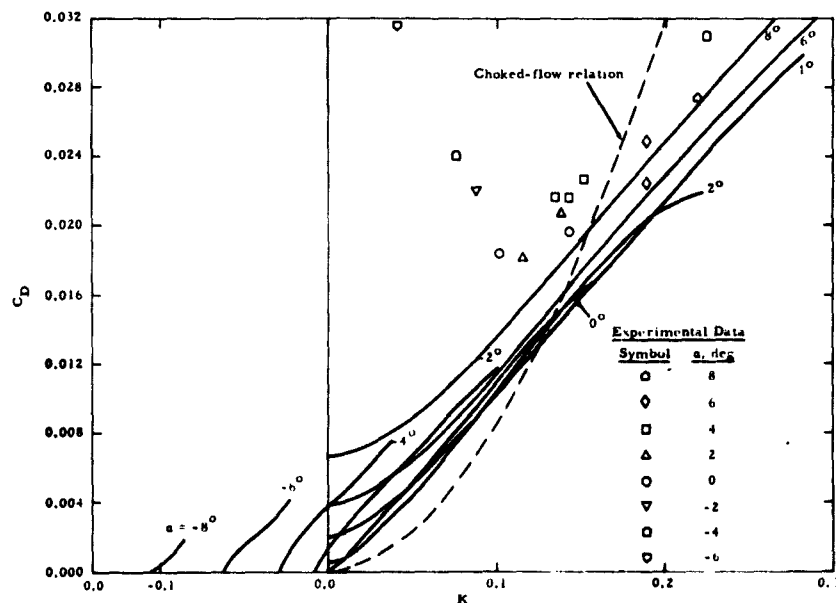


FIG. 24. Theoretical  $C_D$  Versus  $K$  for Hydrofoil B,  $e = 0.3$ , for Various  $\alpha$  Values, and Comparison With Experiment. Closed model.

## Part I

Consider first the dashed curves in Fig. 20 and 23. These give the exact theoretical choked-flow relation between  $C_D$ ,  $K$ , and tunnel height-to-chord ratio,  $\tau$ , from Ref. 6:

$$(36) \quad C_D = (\sqrt{1 + K} - 1)^2 \tau$$

For the tests of Ref. 5,  $\tau = 14/4 = 3.5$ . Since the open data points in the figures are apparently for choked or nearly choked flow, as discussed later, the large departure of those experimental  $C_D$  values from the dashed curves shows that important discrepancies are present between the real and the ideal flow conditions. Boundary-layer separation on the unvented lower side appears to be a major cause of the increase of  $C_D$  as  $\alpha$  decreases from zero. This explanation is suggested by the similar increase of  $C_D$  for fully wetted flow, seen in Fig. 12 of Ref. 5, where, for example,  $C_D$  for  $\alpha = -6.4$  degrees is higher by about 0.0084 than it is for  $\alpha = 0$ . Furthermore, with venting it seems reasonable to expect more forward boundary-layer separation on the lower side, and comparison of the lower-surface pressure distributions with and without venting in Fig. 30 of Ref. 5 seems to support this idea. Finally, if the experimental  $C_D$  values are reduced by 0.0059 to allow for skin friction, as suggested in Ref. 5, page 106, the remaining separation of the  $C_D$  values for large  $\alpha$  from the choked-flow curve may be due to the effect of blockage on the experimental  $K$  determination, as discussed in Ref. 5 (page 104).

There are several reasons for describing the fully vented conditions in the tests of Ref. 5 as being apparently choked flow. First there is the characteristic behavior of  $K$  versus gas supply (Fig. 28 of Ref. 5). More conclusive, however, is the notably linear variation of  $K$ ,  $C_L$  and  $C_M$  versus  $\alpha$  (or  $\alpha$ ,  $C_L$  and  $C_M$  versus  $K$ ) as seen in Fig. 56, 7, and 13, respectively of Ref. 5. That this behavior is precisely that of choked flow can be seen as follows. As long as cavity length is constant--as it is of course in choked flow when  $l = \infty$ --then as  $\alpha$  is varied by adding the flat plate solution for  $\Delta\alpha$ ,  $K$ ,  $C_L$  and  $C_M$  will vary linearly with  $\alpha$ .

A third possible cause of discrepancy between theory and experiment is as follows. A key difference between the experiments of Ref. 5 and previous vented-flow tests is the exhausting of gas at an arbitrary chordwise position on the profile without any sharp edge from which the free streamline springs clear of the profile. Thus the theoretical gas-water interference is often actually a layer of individual bubbles near the exhaust point, as seen in Fig. 21 of Ref. 5. In other words, particularly for negative  $\alpha$  and exhaust ahead of the maximum thickness, some differences are to be expected as the result of the free-streamline separation being delayed till some point aft of the exhaust point.

The last items of experimental data to be discussed are the data points with  $x$  inside and the "tracks" joining the clear and the  $x$  data

points in Fig. 20 and 21. In Ref. 5, the x data identify partially vented flow based on visual observation, and the "tracks" indicate unsteady forces. A definite question about the visual classification of cavity length is implied by the agreement of the slopes of the full-cavity theory and the "track" data up to  $K \approx 0.3$ , where corresponding jogs in the experimental  $C_L$  curves and slope changes in the  $C_D$  curves seem to occur. This suggests that the lower K portions of the "track" data, including some of the x data points, correspond to full-cavity flow.

In discussing this seeming conflict of the visual and theoretically implied indications of flow configuration with the authors of Ref. 5, the following hypothesis was developed. Figure 25 shows the typical sequence of flow configurations observed in the tests of Ref. 5 for increasing and decreasing gas supply. It is believed that configurations B and E can have appreciably different gas supply rates, E being the lower, and yet that they are essentially the same with respect to cavity pressure and hydrodynamic coefficients. However, they would be classified visually as partially vented and full-cavity flow, respectively. Thus the hypothesis is that the lower K portions of the "track" data of Ref. 5 effectively correspond to full-cavity flow, despite the visual classification, and that the qualitative agreement with the full-cavity theory is to be expected. Related behavior has occurred in other cases of clear and frothy cavities, for example as reported in Ref. 8, where the theoretical and the measured drags continue to agree as the cavity becomes frothy and then becomes essentially a separated flow region filled with bubbly water, as reported in Ref. 9.

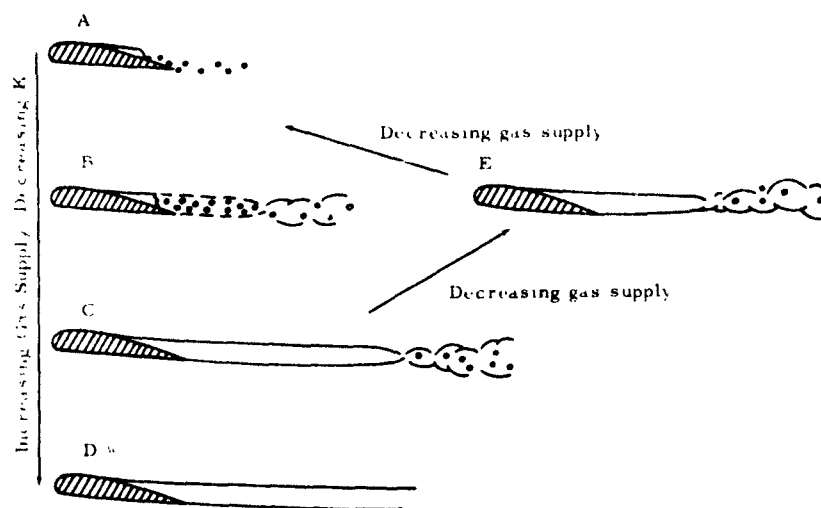


FIG. 25. Sequence of Experimental Cavity Configurations for Increasing and Decreasing Gas Supply.

## SUMMARY

The example calculations, comparisons of theory with experiment, and function tables in this report are the culmination of a study of the linearized theory of vented hydrofoils in two-dimensional flow.

The tables simplify the lift and drag calculations for nearly arbitrary hydrofoil profiles and typical exhaust locations for infinite or finite cavity length of full cavity flow. Moment coefficient, because of its greater calculation complexity, is treated only for infinite cavity length.

Two experimental hydrofoils have been treated with the theory to illustrate the calculation procedure and the nature of the theoretical curves of  $C_L$  and  $C_D$  versus  $K$  and  $\alpha$  for  $e = 0.3$ . The resultant agreement of theory and experiment is poorer than expected from previous comparisons. However, the main discrepancies are reasonably attributed to hitherto less important real-fluid and tunnel-choking effects. In particular, boundary-layer separation on the lower, unvented side seems to have been appreciable for negative attack angles, possibly aggravated by the upper side venting.

While no definite statement about the importance of the choked-flow effects upon the present comparisons can be made until choked-flow-theory calculations are completed, the experimental data display qualitative features of choked flow. The indication of greater effects of choking than noticed before seems reasonable in view of the lower tunnel height-to-chord ratio and the lower theoretical cavity lengths for unbounded flow for the experimental choked flow cavity numbers.

An unexpected result of the comparison for Hydrofoil A is a new interpretation of the visual classification of the experimental flows as fully vented or partially vented, following from the qualitative agreement of portions of the data for so-called partially vented flow with full cavity theory.



## Appendix A

### CORRIGENDA

Since this report completes the theoretical work on vented hydrofoils of Ref. 1, 2, 3, and 10, errors that have been noted in two of those reports are corrected here.

- Item 1: In Ref. 2, page 15, the coefficient of  $d_2$  in the  $C_M$  formula should be  $2(1 + 6 \cos^2 \theta')$  instead of  $2 \cos^2 \theta'(5 + 2 \cos^2 \theta')$ .
- Item 2: In Ref. 2, page 18, each of the group of five formulas for  $(a)C_D = 0$ , labeled Case IIa through IVb, should be reversed in sign.
- Item 3: In Ref. 10, page 5, the formula for  $-C_M/a$  is incorrect\* and should read

$$-\frac{C_M}{a} = \frac{\pi}{2} \left( \frac{1 + \sqrt{e}}{2} \right)^4 \left[ 1 + 4 \left( \frac{1 - \sqrt{e}}{1 + \sqrt{e}} \right)^2 \right]$$

The corresponding curve on the same page should be change accordingly. The corrected curve rises slightly above the straight line that would connect the end points, which remain unchanged, rather than slightly below as given. Also, the corresponding flat-plate term in the  $C_M$  formula for an arbitrary profile on page 6 should be changed to read

$$C_M = C_M^0 - \frac{\pi}{2} a \left( \frac{1 + \sqrt{e}}{2} \right)^4 \left[ 1 + 4 \left( \frac{1 - \sqrt{e}}{1 + \sqrt{e}} \right)^2 \right]$$

- Item 4: In Ref. 10, page 7, the factor  $2/\pi$  in the  $\sqrt{C_D^0}$  formula should be  $\sqrt{2/\pi}$  and the coefficient of  $\int_0^\pi h \left( \frac{\cos \theta - a}{1 + a} \right) d\theta$  in the  $C_M^0$  formula should be  $a/(1 + a)^3$  instead of  $a(1 + 2a^2 - 2a^4)/(1 + a)^3$ .

---

\* Suggested by C. J. Henry of Davidson Laboratory, Stevens Institute of Technology.

## Appendix B

## VENTED WEDGE

The vented wedge is almost as simple as the flat plate to treat for finite  $l$ , because again point singularities on the unit circle produce the solution.

From work reported in Ref. 2, the smooth-entry solution for the vented edge for  $l = \infty$  is seen to be

$$w_s(\zeta) = \frac{\delta}{\pi} \log_e \left( \frac{\zeta - e^{i\theta'}}{\zeta - e^{-i\theta'}} \right)$$

giving

$$\text{Re. } [w_s(\zeta_1)] = u_{c_s} = 0$$

and

$$\begin{aligned} -\text{Im. } [w_s(e^{i\theta})] &= \delta - \alpha_s = \frac{\delta}{\pi} (\pi - \theta'), \quad 0 \leq \theta < \theta' \\ &= -\alpha_s = \frac{\delta}{\pi} (-\theta'), \quad \theta' < \theta \leq \pi \end{aligned}$$

Thus for finite  $l$  the open-model, smooth-entry solution  $w_s(\zeta)$  with  $w_s(\zeta_{\infty}) = 0$  is

$$w_s(\zeta) = \frac{\delta}{\pi} \left[ \log_e \left( \frac{\zeta - e^{i\theta'}}{\zeta - e^{-i\theta'}} \right) + \log_e \left( \frac{\zeta_{\infty} - e^{-i\theta'}}{\zeta_{\infty} - e^{i\theta'}} \right) \right]$$

By taking

$$\frac{\zeta_{\infty} - e^{-i\theta'}}{\zeta_{\infty} - e^{i\theta'}} = \frac{c - a + i(d + \sqrt{1 - a^2})}{c - a + i(d - \sqrt{1 - a^2})} = \frac{[(c - a)^2 + (d + \sqrt{1 - a^2})^2]^{\frac{1}{2}} e^{i\psi}}{[(c - a)^2 + (d - \sqrt{1 - a^2})^2]^{\frac{1}{2}} e^{i\psi'}}$$

where

$$\tan \psi = \frac{d + \sqrt{1 - a^2}}{c - a}, \quad \tan \psi' = \frac{d - \sqrt{1 - a^2}}{c - a}$$

there is obtained

$$\begin{aligned} -\text{Im.} [w_s(e^{i\theta})] &= \delta - \alpha_s = \frac{\delta}{\pi} (\pi - \theta' + \psi' - \psi), \quad 0 \leq \theta < \theta' \\ &= -\alpha_s = \frac{\delta}{\pi} (-\theta' + \psi' - \psi), \quad \theta' < \theta \leq \pi \end{aligned}$$

and

$$\text{Rl.} [w_s(\zeta_1)] = u_{cs} = \frac{\delta}{2\pi} \log_e \left[ \frac{1 + (\tan \psi)^2}{1 + (\tan \psi')^2} \right]$$

Proceeding as usual, with  $\zeta_\infty = (a + ib) = Ne^{i\nu}$ , it is found that

$$t_{ws} + i \frac{C_{Ls}}{2} = 2\pi \frac{dW}{d\zeta} \bigg|_{\zeta_\infty} \frac{d\zeta}{dZ} \bigg|_0 = \frac{\delta l \sqrt{1-a^2}}{N} (\sin \nu + i \cos \nu)$$

Though the mapping for  $l > 1$  is singular for  $l \rightarrow 1$ , the  $s$ -parameters are not. Ordinary procedures show that the limit values for  $l = 1$  are

$$\begin{aligned} \frac{\pi u_{cs}}{\delta} &= \frac{1}{2} \log_e \left[ \frac{1 + \left( \sqrt{\frac{1+\sqrt{e}}{1-\sqrt{e}}} + \sqrt{\frac{2\sqrt{e}}{1-\sqrt{e}}} \right)^2}{1 + \left( \sqrt{\frac{1+\sqrt{e}}{1-\sqrt{e}}} - \sqrt{\frac{2\sqrt{e}}{1-\sqrt{e}}} \right)^2} \right] \\ \frac{\pi \alpha_s}{\delta} &= \tan^{-1} \left( \sqrt{\frac{1+\sqrt{e}}{1-\sqrt{e}}} + \sqrt{\frac{2\sqrt{e}}{1-\sqrt{e}}} \right) - \tan^{-1} \left( \sqrt{\frac{1+\sqrt{e}}{1-\sqrt{e}}} - \sqrt{\frac{2\sqrt{e}}{1-\sqrt{e}}} \right) \\ \frac{t_{ws}}{\delta} &= e^{\frac{1}{4}} \sqrt{\frac{1+\sqrt{e}}{2}}, \quad \frac{C_{Ls}}{2} = e^{\frac{1}{4}} \sqrt{\frac{1-\sqrt{e}}{2}} \end{aligned}$$

The  $s$ -parameter integrals for the vented wedge, with  $\nu = \delta$  on the upper wetted surface and  $\nu = 0$  on the lower, are easily seen to be

$$\begin{aligned} \pi u_{cs} + i\pi \alpha_s &= \delta \int_0^{\theta'} (F_1 + i F_2) d\theta \\ t_{ws} + i \frac{C_{Ls}}{2} &= \frac{bl}{N} e^{-i\nu} \delta \int_0^{\theta'} (F_3 + i F_4) d\theta \end{aligned}$$

Figure 26 compares the analytic and planimeter results for  $e = 0.5$ . Thus the integral forms are checked and the over-all accuracy of the

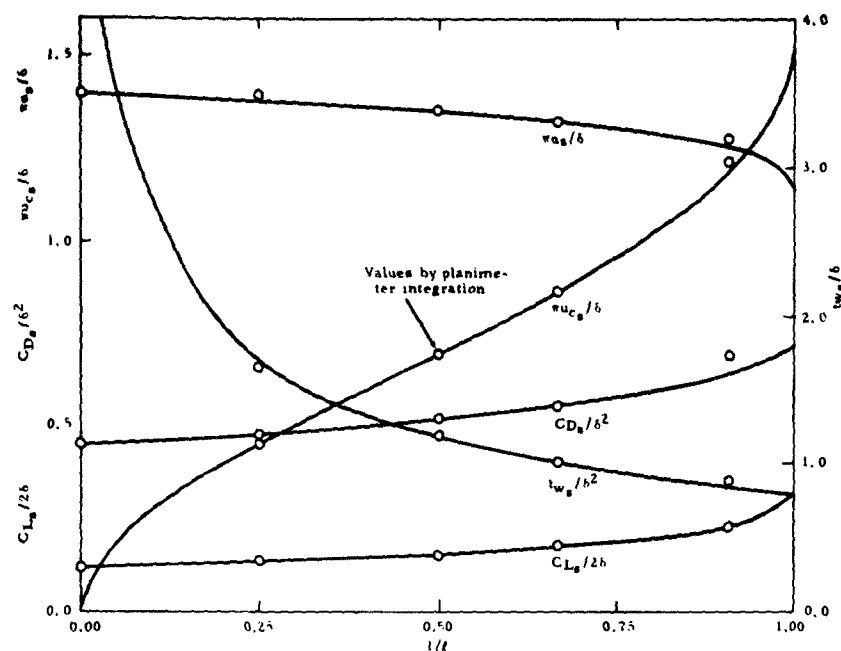


FIG. 26. Analytically Calculated s-Parameters Versus  $1/l$  for Vented Wedge, for  $e = 0.5$ , and Comparison With Planimeter Results.

planimeter calculation procedure is demonstrated. As usual, the curves to be integrated were plotted on 8- by 10.5-inch paper with  $0 \leq \theta \leq 180^\circ$  along 18 centimeters of the longer side. Thus the wedge check on accuracy is believed pessimistic, since  $H = 0$  for  $\theta > \theta' \approx 60^\circ$ . The loss of accuracy for  $l = 1.1$  is due to the fact that nearly equal areas of opposite sign happen to be involved. Because fairing of the curves was a much greater cause of error than the planimeter itself, the additional  $\theta$  values that typically had to be considered in treating the more complex  $H$  or  $\bar{H}$  functions also probably increased the accuracy. However, for future work, a basic interval of 5 degrees would be recommended.

Because the wedge solution for the full range  $1 \leq l \leq \infty$  has been reached, it serves as a useful example for considering the coverage in  $K$  and  $\alpha$  of the proper open and closed models, according to the criterion from Ref. 1 that  $\alpha \geq \alpha^+$ . Thus Fig. 27 gives the cusp-closure parameters for  $e = 0.5$ , and Fig. 28 shows how for each  $l$  the proper solutions cover the line

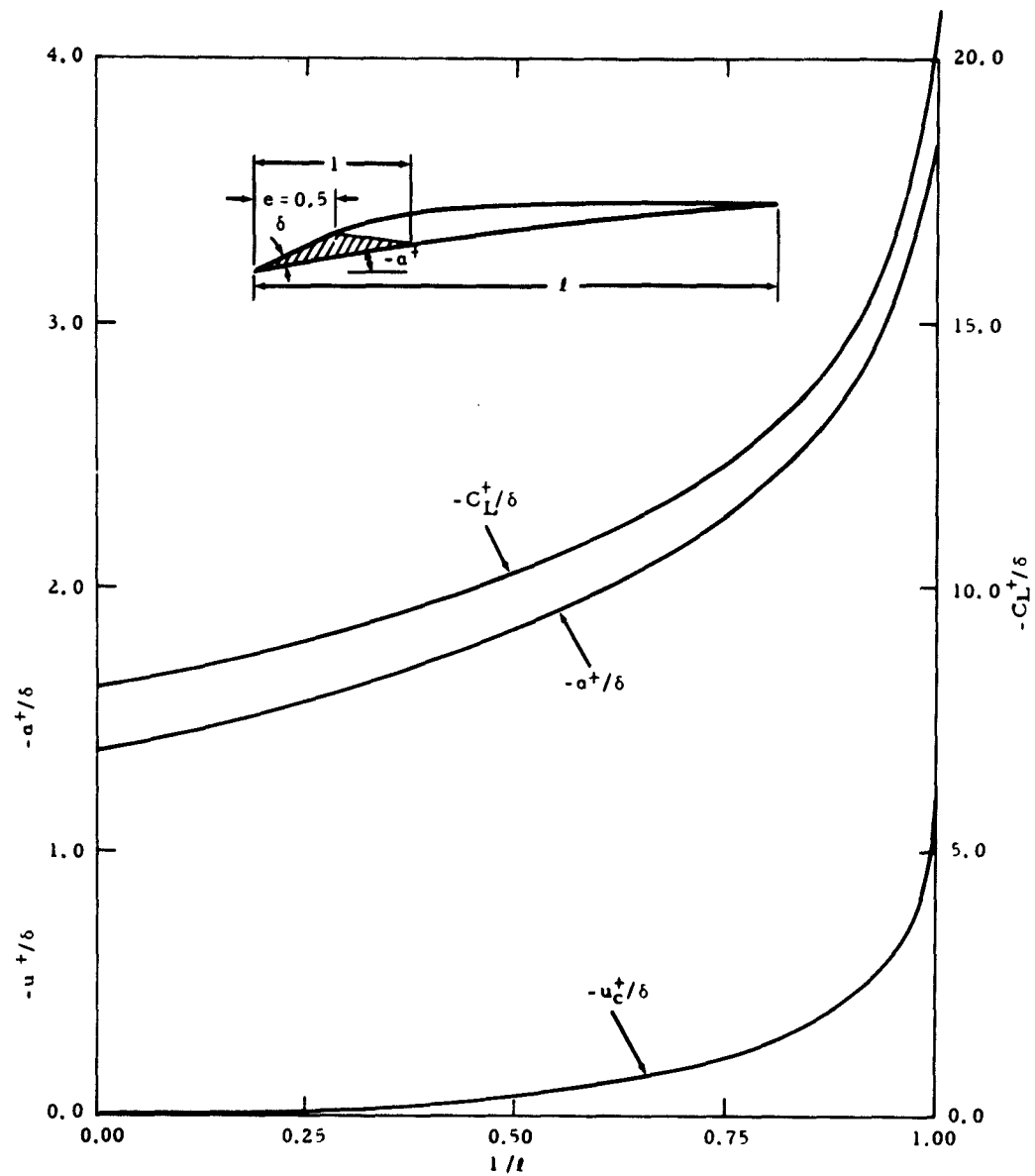
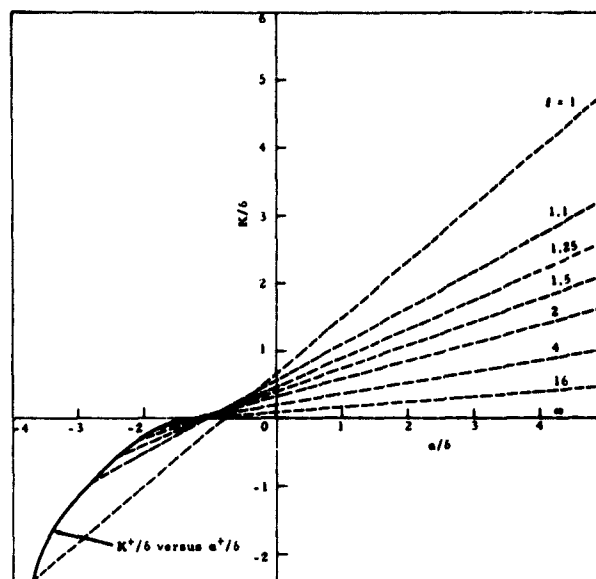
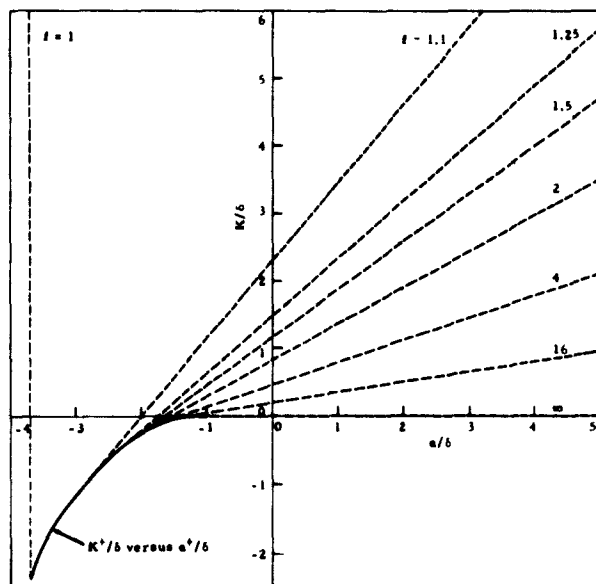


FIG. 27. Cusp-Closure Parameters for Vented Wedge,  $e = 0.5$ .



(a) Open model



(b) Closed model

FIG. 28.  $K, a$  Domain for Proper Solution for Vented Wedge,  $e = 0.5$ .

$$\left(\frac{K}{\delta}\right)_{o, cl} = \frac{K^+}{\delta} + 2 \left(\frac{a - a^+}{\delta}\right) u_{cP, Q}$$

The open-model's multivaluedness for the typically unimportant area of  $a$  near  $a^+$  means that a given  $K$  and  $u$  can be obtained with more than one value of  $l$ , for which the hydrodynamic coefficients will also differ somewhat. Actually the criterion for solution admissibility of  $a \geq a^+$  is not a clear-cut condition since the implied free streamlines should be calculated and any cases where the free streamlines cross even for  $a$  slightly greater than  $a^+$  should be excluded. That such cases occur is suggested by considering the shape of the free streamlines for cusp-closure, as follows. Since the profile-plus-cavity obstacle keeps the same pressure distribution if the free stream is considered reversed, it would appear that for  $u_c^+$  positive, as sometimes occurs, the free streamlines should initially diverge from the cusp in a crossing manner. However, such details have not been found important in the practical application of the theory.

In a more practical respect, only solutions for  $K \geq 0$  are of interest for cavitating flows and even then only if pressure coefficient on the foil nowhere falls below  $-K$ . For vented flows, for which cases of negative  $K$  can be conjectured, it remains to be seen whether real fluid effects will not prevent such cases from occurring, even if both the linearized theory and corresponding nonlinearized potential-flow solutions are spatially reasonable, as in the case of some cusp-closure cavities.

## Appendix C

PARTLY CLOSED MODEL SOLUTIONS FOR  
VENTED FLAT PLATE

As discussed in Ref. 1, for each vented hydrofoil profile there exists a family of partly closed cavity model solutions for given cavity length, with wake thickness  $t_w$  lying between the zero of the closed model and  $t_{w0}$  of the open model. The particular case of the vented flat plate with  $e = 0$  is considered here in order to compare the theoretical ranges of cavity length and wake thickness with certain experimental results given in Ref. 11.

The partly closed model solution for unit angle of attack for each particular cavity length is constructed by superposing the open- and closed-model solutions  $w_P$  and  $w_Q$  with

$$w = T w_P \text{ and } (1 - T) w_Q$$

$$t_w = T t_{wP}, \quad u_c = T u_{cP} + (1 - T) u_{cQ}$$

and with the z-plane closure-singularity strength

$$C_z = (1 - T) \sqrt{C_{DQ}} / 2\pi$$

Consideration of the implied cavity and wake geometry and the drag integral shows that the drag coefficient for the partly closed model is

$$\begin{aligned} C_D &= t_w 2u_c + 2\pi(C_z)^2 \\ &= T t_{wP} 2 \left[ T u_{cP} + (1 - T) u_{cQ} \right] + (1 - T)^2 C_{DQ} \end{aligned}$$

The lift superposition is simply

$$C_L = T C_{LP} + (1 - T) C_{LQ}$$

and since  $C_D/a^2 = C_L/a$  for the flat plate with  $e = 0$ , it must also be (as was found for  $e = 1$  in Ref. 3 and was stated for all  $e$  in Ref. 1) that

$$C_D = T C_{DP} + (1 - T) C_{DQ}$$

This is confirmed by application of the formulas given earlier for the open- and closed-model solutions for  $e = 0$ .



It is not clear from the resultant partly closed model relations, which give  $K$  and  $t_w$  as functions of  $l$  and  $T$ , and which imply  $t_w$  as a function of  $T$  and  $K$ , that maximum wake thickness for given  $K$  corresponds to the open-model limit. However, manipulation of the relations yields

$$\begin{aligned} \left. \frac{\partial t_w}{\partial T} \right|_K &= -\frac{\pi}{2} \sqrt{T} \left( 1 + \frac{T}{2l} \left. \frac{\partial l}{\partial T} \right|_K \right) \\ &= -\frac{\pi}{2} \sqrt{T} (1 - T) \left( \frac{1 + \sqrt{T} \sqrt{T-1}}{l-1} \right) \left[ T + (1 - T) \left( \frac{1 + \sqrt{T} \sqrt{T-1}}{l-1} \right) \right]^{-1} \end{aligned}$$

From this it can be seen that  $t_w$  monotonically increases with  $T$  for constant  $K$ , reaching a maximum and critical point for  $T = 1$ .

To illustrate the partly closed model results, Fig. 29 gives the curves of force coefficient, cavity length, and wake thickness versus cavity number for  $T = 0, 1/2$ , and  $1$ . In Fig. 30 some portions of the same cavity-length and wake-thickness curves are compared with some experimental results of T. E. Dawson, who tested a flat plate for  $e = 0$  (Ref. 11). The upper portion of Fig. 30 shows that the experimental cavity lengths correspond to  $T \approx 3/4$ . If the shortness of the cavities is due to the wake produced by the required gas supply, rather than to the effects of gravity, the free surface, or the bottom of the tunnel, then the experimental gas supply rates should be compatible, at least roughly, with the wake thicknesses corresponding to  $T \approx 3/4$ . The lower half of Fig. 30 shows the experimentally required gas-supply coefficients,  $C_Q$ , which are apparently from the same tests as for the  $l$  measurements. The definition of  $C_Q$  in Ref. 11 makes it correspond to  $t_w/a$ , since

$$C_Q = \frac{Q}{U_\infty bc \sin \alpha}$$

where

$Q$  = volume of gas supplied to test hydrofoil per unit time (reference pressure and temperature assumed very nearly equal to free-stream pressure at hydrofoil depth and water temperature)

$b$  = hydrofoil span

$c$  = hydrofoil chord

In the lower half of Fig. 30, the experimental  $C_Q$  values are seen to correspond more nearly to  $T \approx 1/4$  than to  $3/4$ , but in view of the crudeness of the wake model, the order-of-magnitude agreement seems significant. Also, since the real wake near the cavity is a mixture of gas and water moving downstream relative to the foil at a speed less

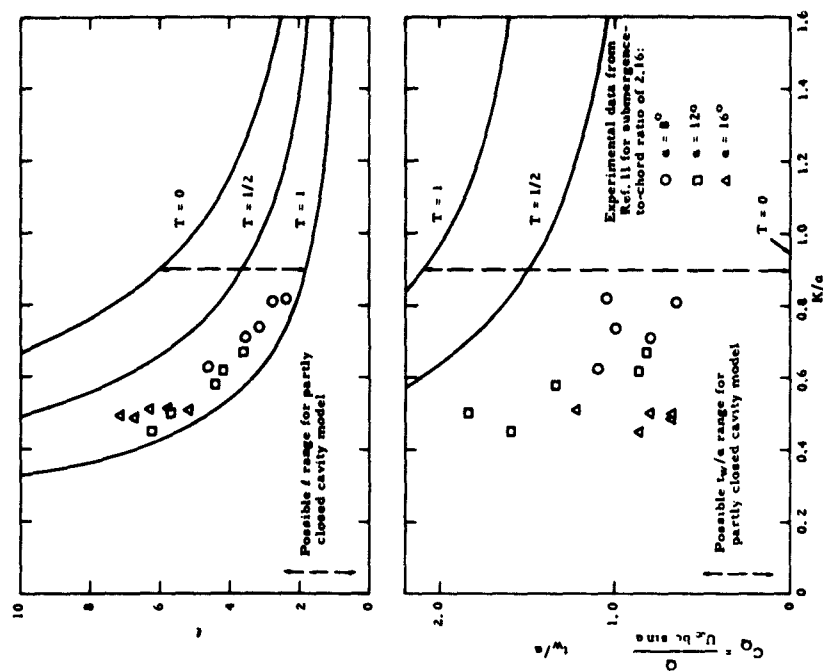


FIG. 30. Comparison of Experimental and Theoretical Cavity Lengths for a Vented Flat Plate,  $e = 0$ , and of Experimental Gas Supply Coefficient and Theoretical Wake Thickness.

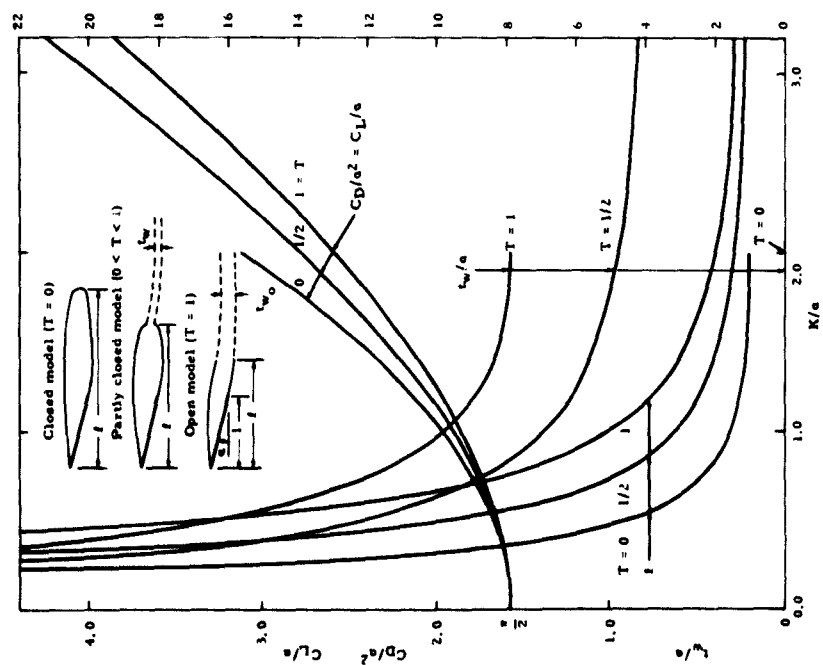


FIG. 29. Force Coefficients, Cavity Length, and Wake Thickness for Partly Closed Model Solution Family for Vented Flat Plate,  $e = 0$ .

than  $U_\infty$ , it is to be expected that the wake thickness implied by gas supply would be smaller than that implied by the hydrodynamic effect of the wake.

It will be interesting to see whether future experiments show other cases of peculiarly short cavities coupled with gas-supply coefficients of the order of  $t_{w0}/4 \approx C_D/4K$ , in accord with the partly closed cavity model interpretation of Dawson's results.

#### REFERENCES

1. Fabula, A. G. "Thin-Airfoil Theory Applied to Hydrofoils With a Single Finite Cavity and Arbitrary Free-Streamline Detachment." J FLUID MECH, Vol. 12, Part 2 (1962), pp. 227-40.
2. U. S. Naval Ordnance Test Station. Theoretical Lift and Drag on Vented Hydrofoils for Zero Cavity Number and Steady Two-Dimensional Flow, by A. G. Fabula. China Lake, Calif., NOTS, 4 November 1959. (NAVORD Report 7005, NOTS TP 2360.)
3. -----, Application of Thin-Airfoil Theory to Hydrofoils With Cut-Off Ventilated Trailing Edge, by A. G. Fabula. China Lake, Calif., NOTS, 13 September 1960. (NAVWEPS Report 7571, NOTS TP 2547.)
4. Abbott, I. H., and A. E. Von Doenhoff. Theory of Wing Sections. New York, Dover, 1959.
5. U. S. Naval Ordnance Test Station. Water-Tunnel Tests of Hydrofoils With Forced Ventilation, by T. G. Lang, D. A. Daybell, and K. E. Smith. China Lake, Calif., NOTS, 10 November 1959. (NAVORD Report 7008, NOTS TP 2363.)
6. Birkhoff, G., M. Plesset, and N. Simmons. "Wall Effects in Cavity Flow - I." QUART APPL MATH, Vol. VIII, No. 2 (July 1950), pp. 151 - 168.
7. The RAND Corporation. Linearized Theory of Cavity Flow in Two-Dimensions, by B. R. Parkin. Santa Monica, Calif., RAND, 15 July 1959. (P-1745.)
8. California Institute of Technology. Water Tunnel Investigation of Two-Dimensional Cavities, by R. L. Waid. Pasadena, Calif., CIT, September 1957. (CIT Hydrodynamics Laboratory Report E-73.6.)

## **NAVWEPS REPORT 7941**

---

### **Part I**

9. California Institute of Technology. Incipient Cavitation and Wake Flow Behind Sharp-Edged Disks, by R. W. Kermeen and B. R. Parkin. Pasadena, Calif., CIT, August 1957. (CIT Engineering Division Report 85. 4.)
10. U. S. Naval Ordnance Test Station. Linearized Theory of Vented Hydrofoils, by A. G. Fabula. China Lake, Calif., NOTS, 7 March 1961. (NAVWEPS Report 7637, NOTS TP 2650.) Also in: Office of Naval Research. Washington, ONR, 18 - 20 April 1961. (ONR-9, Vol. 3.)
11. California Institute of Technology. An Experimental Investigation of a Fully Cavitating Two-Dimensional Flat Plate Near a Free Surface, by T. E. Dawson. Pasadena, Calif., CIT, 1959. (Guggenheim Aeronautical Laboratory, Aeronautical Engineer Thesis.)

INITIAL DISTRIBUTION

- 10 Chief, Bureau of Naval Weapons
  - DLI-31 (2)
  - R-12 (1)
  - RAAD-3 (1)
  - RRRE (1)
  - RRRE-4 (1)
  - RU (1)
  - RUTO (1)
  - RUTO-32 (2)
- 6 Chief, Bureau of Ships
  - Code 106 (1)
  - Code 335 (1)
  - Code 421 (2)
  - Code 442 (1)
  - Code 664 (1)
- 1 Chief of Naval Operations
- 3 Chief of Naval Research
  - Code 429 (1)
  - Code 438 (1)
  - Code 466 (1)
- 5 David W. Taylor Model Basin
  - Code 142 (1)
  - Code 500 (1)
  - Code 513 (1)
  - Code 526 (1)
  - Code 580 (1)
- 1 Naval Academy, Annapolis (Librarian)
- 1 Naval Air Development Center, Johnsville
- 1 Naval Aircraft Torpedo Unit, Quonset Point
- 1 Naval Civil Engineering Laboratory, Port Hueneme (Code L54)
- 1 Naval Engineering Experiment Station, Annapolis
- 1 Naval Ordnance Laboratory, White Oak (Library Division, Desk HL)
- 1 Naval Postgraduate School, Monterey (Library, Technical Reports Section)
- 1 Naval Research Laboratory
- 1 Naval Torpedo Station, Keyport (Quality Evaluation Laboratory, Technical Library)
- 1 Naval Underwater Ordnance Station, Newport
- 1 Naval War College, Newport (Institute of Naval Studies)
- 1 Naval Weapons Laboratory, Dahlgren
- 2 Naval Weapons Services Office

## **NAVWEPS REPORT 7941**

### **Part I**

---

- 1 Navy Electronics Laboratory, San Diego
- 1 Navy Mine Defense Laboratory, Panama City
- 1 Navy Underwater Sound Laboratory, Fort Trumbull
- 1 Office of Naval Research Branch Office, Pasadena
- 1 Army Research Office, Durham
- 1 Air Force Office of Scientific Research (Mechanics Division)
- 10 Armed Services Technical Information Agency (TIPCR)
- 1 Director of Defense (R&E) (Office of Fuels, Materials and Ordnance, Byard Belyea)
- 1 Committee on Undersea Warfare
- 1 Maritime Administration (Coordinator for Research)
- 1 Merchant Marine Academy, Kings Point, N. Y. (Head, Department of Engineering)
- 6 National Aeronautics and Space Administration
- 1 National Bureau of Standards (Fluid Mechanics Section, Dr. G. Schubauer)
- 2 National Science Foundation
  - Director (1)
  - Director, Engineering Sciences Division (1)
- 5 British Joint Services Mission (Navy Staff), via BuWeps (DSC)
- 2 Defence Research Member, Canadian Joint Staff (W), via BuWeps (DSC)
- 2 Aerojet-General Corporation, Azusa, Calif., via BuWepsRep
  - J. Levy (1)
  - Library (1)
- 1 Aeronutronic, Newport Beach, Calif. (Library)
- 1 Airesearch Manufacturing Company, Los Angeles (Dr. B. R. Parkin)
- 1 Alden Hydraulic Laboratory, Worcester Polytechnic Institute, Worcester, Mass.
- 1 American Mathematical Society, Providence, R. I. (Editor, Mathematical Review)
- 1 Applied Physics Laboratory, University of Washington, Seattle
- 1 AVCO Research Laboratory, Everett, Mass. (Technical Library)
- 1 Baker Manufacturing Company, Evansville, Wisc.
- 1 Bell Aerosystems Company, Buffalo (Technical Library)
- 1 Brown University, Providence, R. I. (Division of Engineering)
- 1 Bulova Research and Development Laboratories, Inc., Woodside, N. Y.
- 3 California Institute of Technology, Pasadena (Engineering Division)
  - Prof. C. B. Millikan (1)
  - Prof. M. S. Plesset (1)
  - Prof. V. A. Vanoni (1)
- 1 Case Institute of Technology, Cleveland (Department of Mechanical Engineering)
- 1 Clevite Ordnance, Cleveland (Library)
- 1 Colorado State University, Fort Collins (Department of Civil Engineering)
- 1 Convair, San Diego (Engineering Library)
- 1 Convair Hydrodynamics Laboratory, San Diego

- 1 Convair Scientific Research Laboratory, San Diego
- 1 Cornell Aeronautical Laboratory, Inc., Buffalo (Department 410)
- 1 Cornell University, Graduate School of Aeronautical Engineering, Ithaca (Library)
- 2 Davidson Laboratory, Stevens Institute of Technology, Hoboken, N. J.  
A. Suarez (1)  
Dr. J. Breslin (1)
- 1 Douglas Aircraft Company, Inc., Long Beach (Aerodynamics Section)
- 1 Eastern Research Group, New York City
- 1 EDO Corporation, College Point, N. Y. (Library)
- 1 Electric Boat Division, General Dynamics Corporation, Groton, Conn. (Library)
- 1 Engineering Societies Library, New York City
- 1 General Electric Company, Defense Electronics Division, Pittsfield, Mass. (Engineering Librarian)
- 1 General Electric Company, Schenectady (Librarian, LMEE Department)
- 2 Gibbs and Cox, Inc., New York City  
Dr. S. Hoerner (1)  
Library (1)
- 1 Grumman Aircraft Engineering Corporation, Bethpage, N. Y. (Library)
- 1 Harvard University, Cambridge, Mass. (Department of Engineering Sciences)
- 1 Hughes Aircraft Company, Culver City, Calif. (Library)
- 5 Hydrodynamics Laboratory, CIT, Pasadena  
Prof. A. J. Acosta (1)  
Prof. A. T. Ellis (1)  
Prof. T. Y. Wu (1)  
T. Kiceniuk (1)  
Library (1)
- 1 Hydronautics, Inc., Rockville, Md.
- 1 Illinois Institute of Technology, Chicago (Head, Department of Mechanical Engineering)
- 1 Institute of Aerospace Sciences, Inc., New York City (Librarian)
- 1 Johns Hopkins University, Baltimore (Head, Department of Mechanical Engineering)
- 1 Lehigh University, Bethlehem, Pa. (Civil Engineering Department)
- 1 Lockheed Aircraft Corporation, Burbank, Calif. (Library)
- 1 Lockheed Aircraft Corporation, Missiles and Space Division, Palo Alto, Calif. (R. W. Kermeen)
- 2 Massachusetts Institute of Technology, Cambridge  
Department of Civil Engineering (1)  
Department of Naval Architecture and Marine Engineering (1)
- 1 McDonnell Aircraft Corporation, St. Louis (Library)
- 1 Mississippi State University, State College (Aerophysics Department)
- 1 New York State Maritime College, Fort Schuyler (Librarian)
- 1 New York University, Institute of Mathematical Science, New York City
- 1 North American Aviation, Inc., Los Angeles (Technical Library, Department 56)

# NAVWEPS REPORT 7941

## Part I

- 1 Oceanics Incorporated, New York City
- 1 Operations Research, Inc., Los Angeles
- 2 Ordnance Research Laboratory, Pennsylvania State University,  
University Park (Garfield Thomas Water Tunnel)
- 1 Pacific Aeronautical Library of the IAS, Los Angeles
- 1 Reed Research, Inc.
- 1 Rensselaer Polytechnic Institute, Troy, N. Y. (Department of Mathe-  
matics)
- 1 Republic Aviation Corporation, Farmingdale, N. Y.
- 1 Rocketdyne, Canoga Park, Calif. (Library, Department 596-6)
- 1 Rose Polytechnic Institute, Terre Haute, Ind. (Library)
- 1 Society of Naval Architects and Marine Engineers, New York City
- 2 Southwest Research Institute, San Antonio  
Director, Department of Applied Mechanics (1)  
Editor, Applied Mechanics Review (1)
- 1 Stanford University, Stanford, Calif. (Department of Civil Engineer-  
ing, Prof. B. Perry)
- 1 Technical Research Group, Syosset, N. Y.
- 1 The Boeing Company, Seattle (Library, Organization No. 2-5190)
- 2 The Martin Company, Baltimore (Science Technical Library)
- 1 The Rand Corporation, Santa Monica, Calif. (Technical Library)
- 4 The University of Michigan, Ann Arbor  
Department of Civil Engineering (1)  
Department of Engineering Mechanics (1)  
Department of Naval Architecture and Marine Engineering (2)
- 1 The University of Southern California, Los Angeles (Engineering  
Center)
- 1 Thompson Ramo Wooldridge, Inc., Cleveland (Chief Engineering  
Science Group)
- 1 United Technology Corporation, Sunnyvale, Calif. (Technical Library)
- 2 University of California, College of Engineering, Berkeley  
Prof. J. V. Wehausen (1)  
Library (1)
- 1 University of Illinois, Urbana (College of Engineering)
- 2 University of Iowa, Iowa Institute of Hydraulic Research, Iowa City  
Prof. H. Rouse (1)  
Prof. L. Landweber (1)
- 1 University of Kansas, School of Architecture and Engineering,  
Lawrence
- 1 University of Maryland, Institute of Fluid Dynamics and Applied  
Mathematics, College Park
- 1 University of Minnesota, St. Anthony Falls Hydraulic Laboratory,  
Minneapolis
- 1 University of Nebraska, Lincoln (Department of Engineering  
Mechanics)
- 1 University of Notre Dame (Department of Engineering Mechanics)
- 1 University of Wisconsin, Mathematics Research Center, Madison  
(Prof. L. M. Milne-Thomson)
- 1 Vitro Corporation of America, Silver Spring Laboratory (Librarian)



# ABSTRACT CARD

U. S. Naval Ordnance Test Station

Comparison of Theory and . . . (Card 2)

at 30% chord. The theoretical CD and CL curves for two vented hydrofoils with exhaust at 30% chord are compared with water-tunnel test data. The agreement is not as good as in previous comparisons for leading-edge or trailing-edge free-streamline detachment. Real-fluid and tunnel blockage effects are believed to have produced the discrepancies. Because the calculations for arbitrary profile involve functions that are independent of profile form, the

(Over)  
NAVWEPS Report 7941  
Part 1

U. S. Naval Ordnance Test Station

Comparison of Theory and . . . (Card 2)

at 30% chord. The theoretical CD and CL curves for two vented hydrofoils with exhaust at 30% chord are compared with water-tunnel test data. The agreement is not as good as in previous comparisons for leading-edge or trailing-edge free-streamline detachment. Real-fluid and tunnel blockage effects are believed to have produced the discrepancies. Because the calculations for arbitrary profile involve functions that are independent of profile form, the

(Over)  
NAVWEPS Report 7941  
Part 1

U. S. Naval Ordnance Test Station

Comparison of Theory and . . . (Card 2)

at 30% chord. The theoretical CD and CL curves for two vented hydrofoils with exhaust at 30% chord are compared with water-tunnel test data. The agreement is not as good as in previous comparisons for leading-edge or trailing-edge free-streamline detachment. Real-fluid and tunnel blockage effects are believed to have produced the discrepancies. Because the calculations for arbitrary profile involve functions that are independent of profile form, the

(Over)  
NAVWEPS Report 7941  
Part 1

U. S. Naval Ordnance Test Station

Comparison of Theory and . . . (Card 2)

at 30% chord. The theoretical CD and CL curves for two vented hydrofoils with exhaust at 30% chord are compared with water-tunnel test data. The agreement is not as good as in previous comparisons for leading-edge or trailing-edge free-streamline detachment. Real-fluid and tunnel blockage effects are believed to have produced the discrepancies. Because the calculations for arbitrary profile involve functions that are independent of profile form, the

(Over)  
NAVWEPS Report 7941  
Part 1

NAVWEPS Report 7941  
Part 1

function tables that were generated during this work  
are given in Part 2 of this report, bound separately.

NAVWEPS Report 7941  
Part 1

function tables that were generated during this work  
are given in Part 2 of this report, bound separately.

NAVWEPS Report 7941  
Part 1

function tables that were generated during this work  
are given in Part 2 of this report, bound separately.

NAVWEPS Report 7941  
Part 1

function tables that were generated during this work  
are given in Part 2 of this report, bound separately.

# ABSTRACT CARD

<p>U. S. Naval Ordnance Test Station  Comparison of Theory and Experiment for  <u>Vented Hydrofoils. Part 1. Analysis, by Andrew G.  Fabula. China Lake, Calif., NOTS, March 1963.</u>  56 pp. (NAVWEPS Report 7941, Part 1, NOTS  TP 2977, UNCLASSIFIED.</p>	<p>○</p> <p>2 cards, 4 copies</p> <p>(Over)</p>
<p>U. S. Naval Ordnance Test Station  Comparison of Theory and Experiment for  <u>Vented Hydrofoils. Part 1. Analysis, by Andrew G.  Fabula. China Lake, Calif., NOTS, March 1963.</u>  56 pp. (NAVWEPS Report 7941, Part 1, NOTS  TP 2977, UNCLASSIFIED.</p>	<p>○</p> <p>2 cards, 4 copies</p> <p>(Over)</p>
<p>U. S. Naval Ordnance Test Station  Comparison of Theory and Experiment for  <u>Vented Hydrofoils. Part 1. Analysis, by Andrew G.  Fabula. China Lake, Calif., NOTS, March 1963.</u>  56 pp. (NAVWEPS Report 7941, Part 1, NOTS  TP 2977, UNCLASSIFIED.</p>	<p>○</p> <p>2 cards, 4 copies</p> <p>(Over)</p>
<p>U. S. Naval Ordnance Test Station  Comparison of Theory and Experiment for  <u>Vented Hydrofoils. Part 1. Analysis, by Andrew G.  Fabula. China Lake, Calif., NOTS, March 1963.</u>  56 pp. (NAVWEPS Report 7941, Part 1, NOTS  TP 2977, UNCLASSIFIED.</p>	<p>○</p> <p>2 cards, 4 copies</p> <p>(Over)</p>

NAVWEPS Report 7941  
Part 1

ABSTRACT. The work of three preceding reports on the linearized theory of vented hydrofoils is completed by a detailed exposition of the procedure for calculating hydrodynamic coefficients. The basic assumption is steady, plane potential flow with two free streamlines; one detaching at an arbitrary chordwise position and the other detaching at the trailing edge. The single cavity terminates at an arbitrary distance downstream of the trailing edge. The calculation of the key smooth-entry, open-model parameters is illustrated by considering a symmetrical and a cambered profile, each vented

(Contd. on Card 2)

NAVWEPS Report 7941  
Part 1

ABSTRACT. The work of three preceding reports on the linearized theory of vented hydrofoils is completed by a detailed exposition of the procedure for calculating hydrodynamic coefficients. The basic assumption is steady, plane potential flow with two free streamlines; one detaching at an arbitrary chordwise position and the other detaching at the trailing edge. The single cavity terminates at an arbitrary distance downstream of the trailing edge. The calculation of the key smooth-entry, open-model parameters is illustrated by considering a symmetrical and a cambered profile, each vented

(Contd. on Card 2)

NAVWEPS Report 7941  
Part 1

ABSTRACT. The work of three preceding reports on the linearized theory of vented hydrofoils is completed by a detailed exposition of the procedure for calculating hydrodynamic coefficients. The basic assumption is steady, plane potential flow with two free streamlines; one detaching at an arbitrary chordwise position and the other detaching at the trailing edge. The single cavity terminates at an arbitrary distance downstream of the trailing edge. The calculation of the key smooth-entry, open-model parameters is illustrated by considering a symmetrical and a cambered profile, each vented

(Contd. on Card 2)

NAVWEPS Report 7941  
Part 1

ABSTRACT. The work of three preceding reports on the linearized theory of vented hydrofoils is completed by a detailed exposition of the procedure for calculating hydrodynamic coefficients. The basic assumption is steady, plane potential flow with two free streamlines; one detaching at an arbitrary chordwise position and the other detaching at the trailing edge. The single cavity terminates at an arbitrary distance downstream of the trailing edge. The calculation of the key smooth-entry, open-model parameters is illustrated by considering a symmetrical and a cambered profile, each vented

(Contd. on Card 2)

- 1 Vought Aeronautics, Dallas (Engineering Library)
- 1 Webb Institute of Naval Architecture, Glen Cove, N. Y. (Technical Library)
- 1 Westinghouse Electric Corporation. Baltimore (Engineering Librarian)
- 1 Westinghouse Electric Corporation, Sunnyvale, Calif. (Library)
- 1 Westinghouse Research Laboratories, Pittsburgh (Library)